



Universidad de Oviedo

FACULTY OF CHEMISTRY - DEPARTMENT OF PHYSICAL AND ANALYTICAL CHEMISTRY

MASTER THESIS

THEORETICAL STUDY OF TRANSITION
METAL-PHTHALOCYANINES COMPLEXES:
MOLECULAR DYNAMICS SIMULATIONS AND
EXAFS RESULTS

GEMA RAPOSO HERNÁNDEZ



Master Studies in
**Theoretical Chemistry and
Computational Modelling**

SUPERVISED BY

ÁNGEL MARTÍN PENDÁS
JOSÉ MANUEL MARTÍNEZ FERNÁNDEZ

COURSE 2021-2022

Contents

1	Introduction	5
2	Methodology	8
2.1	Molecular Mechanics	8
2.2	Molecular Dynamics	9
2.3	Born Oppenheimer Molecular Dynamics	11
2.4	X-Ray Absorption Spectroscopy	13
2.5	Single and Multiple Scattering	16
2.6	EXAFS Formulation	17
3	Computational Details	20
3.1	Quantum Mechanical Computations	20
3.2	Classical Molecular Dynamics Simulation Details	20
3.3	Born-Oppenheimer Molecular Dynamics	22
3.4	Modifications included in the Force Field.	22
3.5	EXAFS Spectrum Computation	23
4	Results	26
4.1	Previous experimental results	26
4.2	Molecular Dynamics simulations results	29
4.2.1	Average structures from MD simulations: Testing the original Force Field	29
4.2.2	Extension to other transition-metal phthalocyanines	31
4.3	Born-Oppenheimer Molecular Dynamics simulations results	34
4.4	Analysis of the theoretical EXAFS spectra	36
4.4.1	Temporal convergence	36
4.4.2	Convergence of the theoretical spectra with the number of shells and legs	36
4.4.3	Model structure concept	39
4.5	A comparison between Debye-Waller factors	40

4.5.1	Results from MD simulations	40
4.5.2	Analyzing DW factors relationships applied in the experimen- tal fittings	46
4.5.3	Average EXAFS spectra selecting paths	49
5	Conclusions	53
6	Bibliography	55

CHAPTER 1

Introduction

Phthalocyanine (H_2Pc), as well as many metal substituted phthalocyanines, are planar aromatic macro-cycles consisting of four isoindole units joined by four nitrogen atoms, resulting in a tetradentate ligand. Phthalocyanines have an important role in the field of materials science and nanotechnology¹ because of their properties, like the electrical ones and their strong absorption in the visible region. In addition they are thermally and chemically stable and they can support intense electromagnetic radiations.

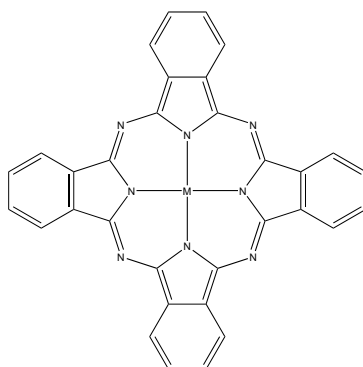


Figure 1.1: Metal phthalocyanine structure.

The size of the metal substituted phthalocyanine depends on the size of the coordinated central atom, which vary within quite a wide range of values.²⁻⁴ The standard oxidation state of Pc is -2, but the oxidation state of the central atom can go from +1 to +5, so it results on a wide variety of possible structures.⁵

Due to the known as *macrocyclic effect*^{6,7} and the high conjugation (18π electrons, aro-

matic system), metal-phthalocyanine complexes show a quite rigid structure despite its large size, that has been extensively studied by various techniques, as XPS, XAS and STM.⁸⁻¹¹

The characterization technique on which this work will focus is *Extended X-ray Absorption Fine Structure* (EXAFS) spectroscopy. This technique is extremely sensitive to the coordination environment of the absorber atom.¹² It is specially relevant in the case of structural determination of species in disordered systems, like solution or non-crystalline media, since it does not require long-range order.¹³

The general formula for the EXAFS spectrum can be expressed as a sum of the contributions to the total amplitude $\chi(k)$ of each backscattering path.^{12,14} Information obtained from EXAFS analysis relies on a set of contributions to the X-Ray absorption coefficient of a given absorber atom coming from the surrounding atoms. That is the reason why this technique is able to provide, specially, structural information around the absorber. The phenomenon is analysed near absorption edges, i.e. energy regions in which the X-ray photon energy matches core electron binding energies. The absorbed photon provokes the ejection of an electron that is treated as a photoelectron, so a wave-like formalism can be applied. The modulation of the absorption coefficient defines what is known as the absorption fine structure, where the EXAFS region can be found, and it is the outcome of a wave interference phenomenon between the outgoing photoelectron and the backscattering waves induced by the atoms around the absorber. The interference pattern depends on the type, number and distance of the scatterer atoms being in the neighbourhood of the absorbing atom. The analysis of that fine structure, therefore, reports basic knowledge about coordination environments. Typically, such process is done on the basis of a non-linear least-squares fitting procedure in which shells around the absorber are identified and parameters defining their respective contributions fitted. Each contribution relies on scattering paths.

The spectra of solid FePc, NiPc, CuPc and ZnPc metal-phthalocyanines have been reported.¹⁵⁻¹⁷ In addition, Carrera et al.¹⁵ also measured 0.1 M aqueous solution of CuPc at 300 K obtaining almost the same results, except for the first coordination shell contribution, which has smaller Debye-Waller factor in solution. Thus, EXAFS spectra can be well described using only intramolecular scattering contributions, neglecting intermolec-

ular ones.

The aim of the present study is the use of theoretical strategies^{18–21} for the generation of EXAFS spectra based on structures obtained from molecular dynamics (MD) simulations trajectories. In order to take into account the intramolecular dynamics, a flexible force field being able to describe the molecular vibrations becomes compulsory. This way of generating spectra is specially interesting, since it allows to check the goodness of the force field. As previously stated, the EXAFS technique is very sensitive to the coordination environment of the absorber atom.

There are some published classical force fields for metal-phthalocyanines. One of them is the published by Chen Shao et al.,²² who developed a Hybrid-COMPASS force field for the CuPc. Dwyer et al.²³ reported a new set of force fields within the CHARMM parametrization model specific to perfluoro-modified MPcs. In particular, our interest goes to the one parametrized for ZnPc. We choose the second force field because its implementation in our software is easier. Within this force field, by introducing some modifications, it is intended to extend it to the other *3d* metals (Fe, Ni, Cu) in order to generate their corresponding theoretical spectra. Therefore, we can test if the model properly reproduces the data reported by the experimentalists.

Additionally, *ab initio* molecular dynamic (AIMD) simulations have also been done in order to check the results of the classical ones. This way of running simulations offers an alternative to the use of classical force fields, but it has the disadvantage of the large amount of computational cost and it is also conditioned by the level of theory and the size of the basis set used. Nonetheless, AIMD results are also reported in this work, what will allow to compare both theoretical strategies.

Finally, it is worth mentioning that one advantage of the theoretical methodology here employed is the fact that no fitting is performed in the process. Therefore, the number of scattering contributions can be as large as needed. This opens the possibility of analyzing the experimental strategies followed when performing the EXAFS fitting, i.e., whether the approximations adopted in terms of the chosen scattering contributions and their respective amplitudes agree with the theoretical results.

CHAPTER 2

Methodology

2.1 Molecular Mechanics

The force field of a molecular system defines the potential energy surface that determines its properties. It is made up of all the parameters that describe the atoms and all the interactions that occur between them, as well as their mathematical treatment.

To develop a force field, we must assume a set of equations and their parametrization. It is very common to define the force field on the basis of two basic contributions: the bonding or covalent interactions and the non-bonding ones. For bonding interactions, the most common contributions defined are *bond stretching*, *bond-angle bending* and *torsion*. Nonbonding interactions usually involve *electrostatic* and *van der Waals interactions*.²⁴ The total energy of the system would be obtained from the sum of all the contributions. However, the presence of other contributions is common in many force fields, such as, for example, the so-called *cross-coupling* terms that define the coupling between the aforementioned linking contributions that, initially, were considered independent. It is also possible to have polarizable force fields, which account for instantaneous variations in charge distribution. Therefore, in order to determine the energy of the system knowing the nuclear coordinates, it is necessary to know the number of bonds, angles and dihedral angles present in the molecule, as well as the atoms involved in each of them. The selection of the set of parameters (force field constants) is based on the ability to reproduce a set of selected properties, whose origin may be either experimental or theoretical.

In the present study, the CHARMM²⁵ force field has been used. The functional form of

the potential energy, U , incorporating the different contributions, is the following:

$$\begin{aligned}
U = & \sum_{bonds} k_b(b - b_0)^2 + \sum_{angles} k_\theta(\theta - \theta_0)^2 + \sum_{dihedrals} k_\phi[1 + \cos(n\phi - \delta)] \\
& + \sum_{impropers} k_\omega(\omega - \omega_0)^2 + \sum_{Urey-Bradley} k_u(u - u_0)^2 + \sum_{nonbonded} \frac{q_i q_j}{\epsilon r_{ij}} \\
& + \epsilon \left[\left(\frac{R_{min_{ij}}}{r_{ij}} \right)^{12} - \left(\frac{R_{min_{ij}}}{r_{ij}} \right)^6 \right]
\end{aligned} \tag{2.1}$$

the first term is for bond stretching, where k_b is the force constant of the bond and b_0 is the equilibrium distance. The second term is the bond-angle bending, where the terms are the equivalent to the bonding ones but for angles. The third term corresponds to the torsion angles, where k_ϕ is the force constant, n is the multiplicity of the function and δ is the phase shift. The fourth term is for impropers, that is, out of plane bending, where k_ω is the force constant and $\omega - \omega_0$ is the out of plane angle. The fifth term is the Urey-Bradley component (cross-term accounting for angle bending, where u is the covalent spring bond), which is not taken into account in the force field used. The last ones are the nonbonded interactions, Coulombic and van der Waals, where $R_{min_{ij}}$ is the well minimum distance, ϵ is the well depth and r_{ij} is the distance between atoms.

The specific parameters of the force field used in this work were developed by Dwyer et al.²³ by fitting a theoretical potential energy surface calculated at the DFT level for ZnPc and derivatives.

2.2 Molecular Dynamics

Classical Molecular Dynamics (MD) is a simulation method where different configurations of the system are generated by integrating Newton's laws of motion simultaneously for all the atoms in the system. To do this, a time discretization is performed, that is, between one configuration and the next one there is a time distance known as *timestep*, typically in the order of tenths of a femtosecond for flexible systems to properly describe molecular vibrations. As a result, a trajectory is generated that specifies the position and velocity of the atoms as a function of time, simulating the microscopic behavior of the system, which allows obtaining both equilibrium and transport properties.

In MD, the energy of the system, H , is a function of the set of coordinates \vec{r} and momenta \vec{p} of all the particles in the system:

$$H = H(\vec{r}, \vec{p}) = K(\vec{p}) + U(\vec{r}) = \sum_i \frac{p_i^2}{2m_i} + U(\vec{r}) \quad (2.2)$$

$K(\vec{p})$ and $U(\vec{r})$ represent the kinetic and the potential energies of the system, while \vec{p}_i and m_i correspond to the momenta and masses, respectively, of the particles i present in the system. In this way, any microscopic state of the system is characterized by a set of values \vec{r}, \vec{p} , which define a point of the so-called *phase space*.

For an isolated system of N particles, the second Newton's Law says:

$$\vec{F}_i(\vec{r}_i \dots r_N) = m_i \frac{d^2 \vec{r}_i}{dt^2} \quad (2.3)$$

where \vec{F}_i is the net force acting on particle i , which is given by the gradient of the potential energy function:

$$\vec{F}_i = -\vec{\nabla} U(\vec{r}) \quad (2.4)$$

In MD simulations, Newton's N differential equations of motion (actually, $3N$ equations for a three-dimensional system) are integrated to project the position of the particles as a function of time and thus be able to generate the trajectory of the complete system. The resolution of the equations is done approximately by means of finite difference methods, which allows the evolution in time of the atomic positions from the successive temporal increments.

The last equation (eq. 2.4) is particularly relevant since it defines the forces that act within the system under study, and therefore, the dynamics that it follows, which ultimately will determine its properties. Precisely at this point appears the connection between the force field concept, covered in the previous section, and molecular dynamics: each simulation step is determined by the differentiation of the potential energy function (eq. 2.4), that is, by the forces that act on the particle at each instant, and that determine its evolution in time. As a consequence, any alteration in the force field, or the use of a different force field, will generate a different trajectory than the original one.

Direct integration over Newton's equations produces a trajectory in the microcanonical ensemble (NVE), in which the number of particles (N), the volume (V) and the total

energy are constant (E). However, it is very common to run simulations under the conditions in which experiments are carried out in the laboratory. We thus find the NVT ensemble, where the energy can vary to keep the average temperature (T) constant, and NPT ensemble, where in addition to having a constant temperature, the volume can be varied so that the average pressure (P) becomes constant. To work in those ensembles, it is necessary to modify the speeds of the particles (which determine the temperature), taking into account the instantaneous deviation from the target temperature (T_0). A common mechanism is to couple a thermostat to the system under study, which enables the exchange of energy with a thermal reservoir (it acts as a thermal bath). To do this, two new terms are added to the original Hamiltonian, which account for the contribution to potential energy and kinetic energy as a consequence of the energy flow between the system and the thermal bath. By choosing the effective mass of the bath, the intensity of the disturbance caused by the coupling with it can be regulated. This type of scheme is the one developed, for example, by the Nosé-Hoover Thermostat,^{26,27} used in this work. To maintain a constant average pressure, a barostat is applied following an equivalent philosophy, but now affecting the volume of the system, which can fluctuate throughout the simulation.

The quality of the results obtained from classical molecular dynamics simulations fundamentally depend on the force field chosen to reproduce the properties of the system. One way to quantify the quality of the force field is to compare the results with the available experimental information, being in this sense the EXAFS spectroscopy a good benchmark due to its high sensitivity to small structural changes.²⁸

2.3 Born Oppenheimer Molecular Dynamics

We have already seen how, through the integration of Newton's equations, we can obtain classical trajectories from MD simulations. For this, it is only necessary to have a force field describing the system we want to simulate. In one hand, the great advantage of classical MD is that it is computationally cheap, but in the other hand, the need for a force field makes simulations strongly dependent on its quality, that is, if a force field has been developed to describe properly certain properties, it may fail to describe others that were not taken into account during its parametrization.

One way to break the dependency on force fields is to use *ab initio* simulations. The increase computational power in recent years make possible to use electronic structure theory directly in simulations.²⁹ This strategy was first proposed by Warshel and Karplus³⁰ and, now, its quality depends on the electronic structure method chosen. It also offers the possibility of study the evolution of reactive systems as it gives an explicit electronic wavefunction description at each step of the simulation.

In order to perform direct dynamic simulations in a potential energy surface for a single electronic state, two approaches are available: Car-Parrinello³¹ (CP) and Born-Oppenheimer (BO) molecular dynamics. In CPMD, the electronic wavefunction and the nuclei motion are propagated simultaneously, while in BOMD, at each step of the trajectory, the potential energy and the gradients are obtained by optimizing the electronic wavefunction. We will focus on BOMD. It is important to know that one assumption on those method is that the system satisfies the Born-Oppenheimer adiabatic approximation, that is, systems in which we can separate the motion of the nuclei and the motion of electrons.

In BOMD simulations, first, for any configuration, we must solve the ground-state electronic problem using one of the available electronic structure methods. The most used in BOMD simulations is the Kohn–Sham (KS) formulation of density functional theory. The forces acting on the nuclei are then obtained via Hellman-Feynman theorem.^{32,33} Once the forces acting on the nuclei are known, we can obtain the evolution in time of the nuclei, as in classical MD, using algorithms as the Verlet one. When the new configuration is achieved, we go to the first step, the calculation of the KS equations for the new configuration of the system. In this way, the nuclei move on the Born-Oppenheimer surface. One way of saving time in the implementation of the algorithm is the extrapolation of the electronic wavefunction from one step to another. The only limitation, as in classical MD, is that the choose of the timestep is limited by the highest frequency of the system. One disadvantage of BOMD respect to CPMD is that the first one need more accuracy on self-consistency, due to the need of obtaining accurate forces. CPMD does not give accurate forces because it propagates simultaneously the nuclei and the electrons, but it results on acceptable average nuclear trajectories.³⁴

In addition to these methods for dynamics simulations, there are formulations applied to MD simulations and based on the time-dependent variational principle³⁵ for the dynamics

of both electrons and nuclei in molecular systems, but those are beyond the objectives of this work.

2.4 X-Ray Absorption Spectroscopy

X-ray Absorption Spectroscopy (XAS) started about one hundred years ago,³⁶ but at the beginning its principles and applications were not very clear. It was in 1971 when Sayers, Stern and Lytle¹⁴ applied Fourier analysis to the point scattering theory, giving rise to X-ray Absorption Fine Structure (XAFS). When the Fourier transformation is applied to the function, a pseudo radial distribution function is extracted, where each peak and its integral gives information about the location of neighboring atoms and the number of them, respectively. Since then, significant progress has been made in the past few decades, especially in the theoretical comprehension of the technique. These theoretical advances went hand in hand with advances in synchrotron radiation X-ray sources and computer technology.³⁷

Nowadays, electromagnetic radiation in the X-ray region, wavelength in the range 0.1 to 50 Å, is the most powerful probe in the structural characterization of matter. When the oscillating electric field of the X-ray radiation interacts with the electrons of the molecules, it can be either scattered or absorbed by these electrons. When a narrow parallel monochromatic X-ray beam of intensity I_0 passes through a sample of thickness x , part of the radiation is absorbed, getting a reduced intensity I . The relationship between both intensities and the sample thickness is given by Beer-Lambert's law:

$$\ln \left(\frac{I_0}{I} \right) = \mu x \quad (2.5)$$

where μ is the linear absorption coefficient, which depends on the atom type and the density of the sample. When the X-ray incident energy increases, the absorption coefficient μ monotonically decreases, being a smooth function of the energy E , whose value depends on the intensity ρ , the atomic number Z and the atomic mass A .

$$\mu = \frac{\rho Z^4}{AE^3} \quad (2.6)$$

However, at a given energy, there is a strong and sharp increase, known as absorption edge. This increment is related to the excitation of an electron in the absorber atom,

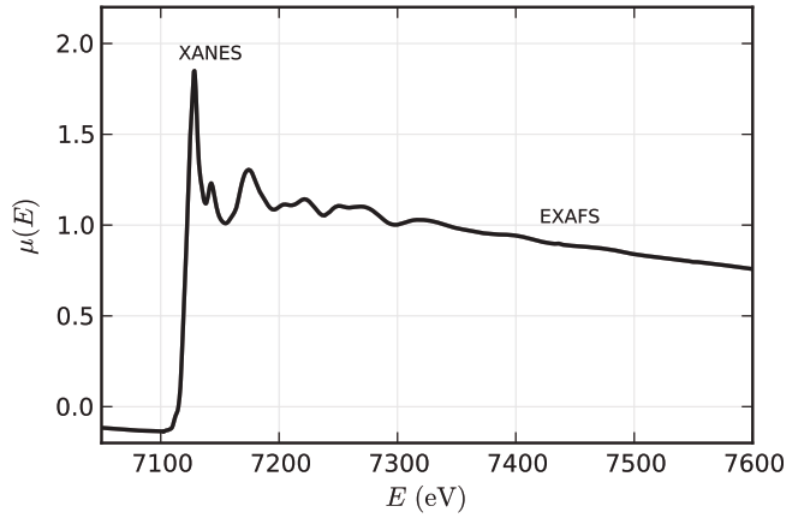


Figure 2.1: XAFS, $\mu(E)$ for the Fe K edge of FeO^{38}

and it occurs when the energy of the incident photons is enough to cause excitation of a core electron of the absorbing atom. The energy needed to excite an electron of the absorbing atom is well known, and it depends on the atom nature and the electronic level from which the atom is extracted ($K=1s$; $L_I=2s$; etc). This means that the phenomenon is local and centered around an absorbing atom and thus dependent on its close surrounding. The most important consequence is that, in principle, the corresponding spectroscopy is applicable to any kind of sample, ordered or not ordered, in gas, liquid or solid phase, and it is strongly dependent on the absorbing atom. This is a great advantage over other structural determination techniques, such as X-ray diffraction (XRD).

The excited state typically decays within a few femtoseconds, as X-ray fluorescence (a higher energy core-level electron fills the deeper core hole, ejecting an X-ray photon) or Auger effect (an electron drops from a higher electron level and a second electron is emitted). Either of these mechanisms are valid to measure the absorption coefficient. A typical XAFS spectrum, where the absorption coefficient is plotted versus the energy, is shown in Figure 2.1

It can be observed that the absorption coefficient does not vary monotonously above the absorption edge, and it is related with the chemical environment of the absorbing atom.

The kinetic energy of the ejected electron is the difference between the energy of the in-

cident photon and the binding energy of the electron. According to wave-particle duality, electrons can be treated as waves, whose wavelength is given by the de Broglie equation:

$$\lambda = \frac{h}{p} \quad (2.7)$$

The wavelength of the excited photoelectron can be expressed as a function of the wave number

$$\lambda = \frac{2\pi}{k} \quad (2.8)$$

$$k = \frac{2\pi}{h} \sqrt{2m(E - E_0)} \quad (2.9)$$

Since X-ray absorption is a transition between two quantum states, the absorption coefficient can be described as a function of the probability of the transition, following the Fermi's Golden Rule³⁹

$$\mu(E) = 4N_a \pi e^2 \left(\frac{\omega}{c} \right) |\langle \Psi_f | \epsilon r | \Psi_i \rangle|^2 \rho(E_F) \quad (2.10)$$

In the equation, $|\langle \Psi_i |$ represents the initial state, and $|\Psi_f \rangle|$ the final state. The initial state (X-ray and a core electron) is well defined, but the final state is a sum of the contributions of the emitted and the backscattered electron. The sum of both wavefunctions would give rise to the fine structure observed in the spectrum, i.e., an specific interference pattern.

Backscattering is produced when the outgoing wave interacts with the neighbours of the absorber atom. Thus, the total wavefunction of the photoelectron increases if the backscattered wavefunction is on phase, and decreases if it is not. The interaction can be with one neighbour and back (single-scattering, SS) or it can be with more than one atom before returning to the absorber (multiple-scattering, MS).

Overall, XAFS spectroscopy is a consequence of the wave nature of the photoelectron. The phase in which the waves are found is related to the distance at which the neighbouring atoms are, and their ability to backscatter. Thus, structural information of the molecule (coordination number, atomic distances) and compositional (nature of the scattering atoms) can be extracted.

Typically, the regions of the spectrum are divided into:

- **XANES:** X-ray Absorption Near Edge Structure lies -10 and 50 eV from the main absorption edge. In this region, MS pathways are especially relevant, mostly those involving the first shell around the absorber. Relatively long pathways are relevant as well. This region is also influenced by the geometrical arrangement of the atoms surrounding the absorber, and can give useful structural information.

The edge position is highly influenced by the oxidation state of the absorbing atom, so that the higher the oxidation state, the more attraction electrons feel for the nucleus, displacing the absorption edge to higher energy values.

- **EXAFS:** Extended X-ray Absorption Fine Structure, it goes typically from 50 eV to 1000 eV over the absorption edge. Unlike the previous region, the kinetic energy of the backscattered photoelectron is high and the processes that predominate are those of simple scattering. It is useful to know bond distances, coordination number and configurational disorder.

2.5 Single and Multiple Scattering

- **Single scattering (SS):** the photoelectron interacts with one atom before returning to the absorber giving information about the distances of the nearest atoms. There are as many paths as coordination spheres. It is said that these paths have two "legs", which represent the way to the backscatter atom and the way back to the absorber.
- **Multiple scattering (MS):** the photoelectron can interact with more than one atom before returning to the absorber. MS pathways are longer than the single backscattering paths from the nearest neighbours, and are particularly important in the low- k XAFS region,⁴⁰ where these processes are more significant. MS paths take on special relevance, reaching the level of SS, in systems in which the absorber atom is aligned or cuasi-aligned with the scattering atoms, that is, in systems with high symmetry. This phenomenon is known as *focusing effect*.^{41,42}

In Figure 2.2 are illustrated some examples of single and multiple scattering paths involved in the MPCs analysis.

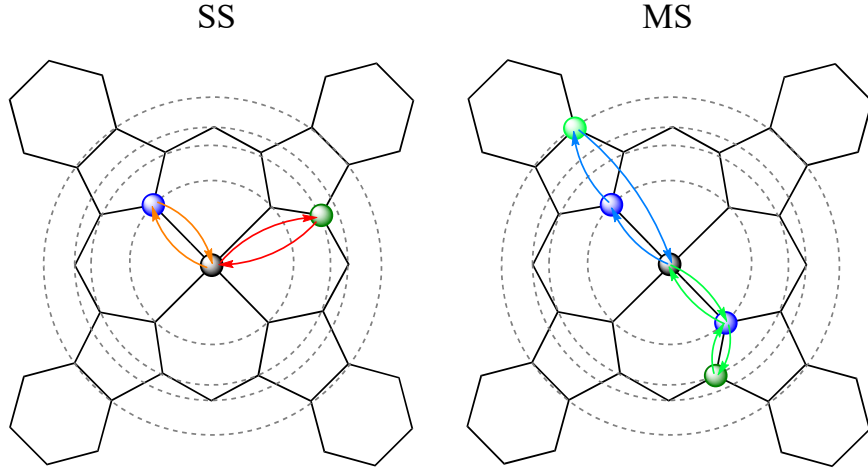


Figure 2.2: Schematic representation of single and multiple backscattering paths. In orange and red, paths with two legs; in blue and green, paths with three and four legs, respectively. The dotted circumferences define the coordination shells.

2.6 EXAFS Formulation

The absorption coefficient above the edge can be described by the following equation:^{43,44}

$$\mu(k) = \mu_0(k)[1 + \chi(k)] \quad (2.11)$$

The oscillatory part of the total absorption, $\chi(k)$, is the result, already mentioned, of the interference of the outgoing photoelectron wave with the one backscattered by neighboring atoms, so it contains information about the local structure around the absorbing atom. Assuming an arrangement around the absorbing atom defined by coordination shells, the EXAFS wave amplitude will be proportional to the number of atoms N_j of the coordination shell (considering that it is formed by atoms of the same type), located at a distance R_j of the central atom. The general form of the EXAFS function is based on the sum of contributions from each considered scattering path j :

$$\chi(k) = \sum_j \frac{N_j}{kR_j^2} F_j^{eff}(k) \sin(2kR_j + \varphi_j(k)) \quad (2.12)$$

where F_j is the effective amplitude function for each scattering path, which has a complex dependency with k , although it varies with the atomic number Z , allowing to distinguish atomic types. The first term of the sine function indicates that the wave is offset by a factor $2kR_j$, where R_j is the distance at which the scattering atom is located, and the

second term defines the phase shift caused by the photoelectron experiencing twice the potential of the absorbing atom and once that of the backscattering atom.

In addition to what has been described so far, there are more factors that modify the EXAFS function that must be taken into account in the analysis of the spectra. One of them is the S_0^2 amplitude reduction factor⁴⁵ :

$$S_0^2 = \prod_i |\langle \Psi'_i | \Psi_f \rangle|^2 \quad (2.13)$$

This factor includes the potential that affects the passive electrons, which are not directly involved in the X-ray absorption process, and which is different when the atom is ionized. $|\langle \Psi'_i |$ and $|\Psi_f \rangle|$ are the wave functions of the passive electrons before and after the X-ray absorption process, respectively. Theoretical calculations show that for high energies ($k > 7 \text{ \AA}^{-1}$), S_0^2 is almost independent of k with a typical value between 0.75 and 0.95, so it is usually treated as a constant scale factor.

Furthermore, it has been considered that the backscattered electron wave is coherent with the outgoing wave, which is essential for the interference process to take place. This is only true during the lifetime of the hole created in the excited atom. This effect is considered by the factor $e^{\frac{-2R_j}{\lambda(k)}}$, which is related to the probability that the photoelectron goes to the backscatter atom and returns to the absorber without inelastic losses and without the hole being occupied. $\lambda(k)$ is the mean free path of the emitted photoelectron.

Finally, it must be considered that atoms vibrate around their equilibrium position (dynamic disorder), and that structural distortions (static disorder) can occur in each coordination shell, even at low temperatures. This means that the atoms may be displaced an amount δR from their average position. The backscattering process occurs on a time scale of $10^{-15} - 10^{-16}$ s, while a molecular vibration occurs in the order of 10^{-13} s. Therefore, the EXAFS function $\chi(k)$ is an average of the contributions from all distances R , between all absorber-backscatter atomic pairs. Due to the aforementioned disorder (Figure 2.3), there is a range of distances, within a shell, between the absorber and the backscatter, which gives rise to a reduction in the amplitude of the signal (which becomes more significant at high values of k). If a Gaussian distribution of the disorder is assumed, it can be taken into account in the EXAFS function by the factor $e^{-2k^2\sigma_j^2}$, where σ_j^2 is the so-called

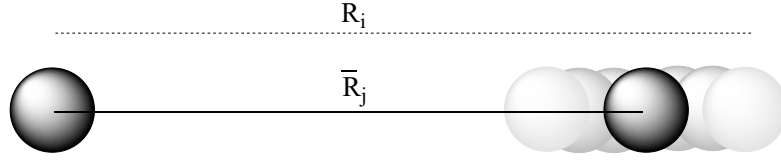


Figure 2.3: Representation of atomic “disorder”. \bar{R}_j represents the average distance between the two atoms and R_i an instantaneous distance.

Debye factor -Waller (DW):⁴⁰

$$\sigma_j^2 = \langle (R_i - \bar{R}_j)^2 \rangle_j \quad (2.14)$$

where \bar{R}_j is the average distance of the shell j and R_i is the instantaneous value of the distance to the absorbing atom. This factor encompasses both static and dynamic disorder.

If all the contributions described are added, the EXAFS formula is:

$$\chi(k) = \sum_j \frac{N_j}{kR_j^2} S_0^2 |F_j^{eff}(k)| e^{-2k^2\sigma_j^2} e^{\frac{-2R_j}{\lambda(k)}} \sin(2kR_j + \varphi_j(k)) \quad (2.15)$$

where, for each backscattering path j , N_j is the coordination number, F_j^{eff} the backscatter amplitude function, S_0^2 is the amplitude reduction factor, \bar{R}_j is the mean absorbent-backscatter distance, φ_j is the phase shift, λ is the photoelectron mean free path, and σ_j^2 is the Debye-Waller factor of the shell.

From an experimental point of view, parameters such as the scattering amplitude function, the phase shift or the mean free path can be obtained by theoretical calculations for each path, indicating only the types of atoms involved, or by model compounds of known structure. Thus, the remaining structural parameters present in the EXAFS equation, such as the absorber-backscatter distance and the DW factor, are obtained by fitting the experimental spectrum.^{28,46,47}

CHAPTER 3

Computational Details

3.1 Quantum Mechanical Computations

The structures of the $3d$ transition-metal phthalocyanines were optimized at MP2 level using 6-311G (d,p)⁴⁸⁻⁵⁰ basis set. Charges fitting was done according to the Merz-Singh-Kollman scheme^{51,52} using UFF radii for atomic charges calculations (MKUFF).

Due to the high computational cost of BOMD simulations, we cannot use the MP2 level of theory. We tested the TPSS⁵³ functional with the same basis set of MP2 calculations (6-311G(d,p)). The validity of the functional has been tested for metals of the $3d$, $4d$ and $5d$ transition series, reproducing properly experimental geometries and vibration frequencies.⁵⁴ The results of the geometry optimization at both levels of theory are collected in Table 3.1. The calculations were performed using ORCA.⁵⁵ The differences between both levels of theory are in the hundredth of an angstrom, which we consider to be acceptable for the aim of this work.

3.2 Classical Molecular Dynamics Simulation Details

Classical Molecular Dynamics (MD) was performed using a modified version of the DLPOLY package.⁵⁶ The simulations were run at temperatures of 80 K and 300 K in the NVT ensemble using a Nosé-Hoover thermostat with $\tau = 0.1$ ps. No cutoff radius was applied to non-bonding interactions.

The total simulation time was 1.1 ns with a chosen time step of 1 fs. There was a first stage of equilibration lasting for 0.1 ns. The production period was extended for 1 ns,

Table 3.1: Distances for the first four shells of MPcs from QM-optimizations. See Fig. 3.1 for shells definition.

FePc	R_1 (Å)	R_2 (Å)	R_3 (Å)	R_4 (Å)
MP2	1.9358	2.9664	3.3770	4.2071
TPSS	1.9331	2.9767	3.3833	4.2110
NiPc	R_1 (Å)	R_2 (Å)	R_3 (Å)	R_4 (Å)
MP2	1.8876	2.9338	3.3630	4.1738
TPSS	1.9044	2.9537	3.3738	4.1893
CuPc	R_1 (Å)	R_2 (Å)	R_3 (Å)	R_4 (Å)
MP2	1.9457	2.9711	3.3789	4.2130
TPSS	1.9578	2.9850	3.3870	4.2250
FePc	R_1 (Å)	R_2 (Å)	R_3 (Å)	R_4 (Å)
MP2	1.9850	2.9968	3.3902	4.2400
TPSS	1.9950	3.0109	3.3962	4.2525

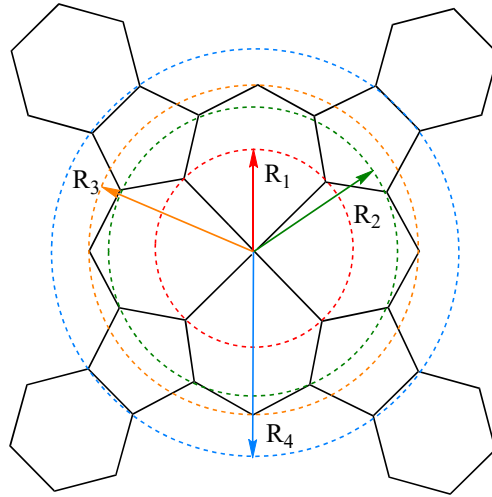


Figure 3.1: Schematic representation of the first four coordination shells distances (R_n).

saving configurations every 2000 steps, obtaining trajectories of 500 snapshots. Another set of simulations were run with a production time of 5 ps, saving configurations every 10 steps, obtaining trajectories of 500 snapshots. The aim of this shorter simulation is to

compare their results with the BOMD ones.

3.3 Born-Oppenheimer Molecular Dynamics

The *ab initio* classical trajectories are computed using ORCA⁵⁵ at TPSS/6-311G(d,p).^{48–50} Strictly, these are Born-Oppenheimer molecular dynamics simulations (BOMD), because they approximately solve the time-independent Schrödinger equation to compute gradients and then move the atoms according to them.

For each complex, the simulations were run at 80 or 300 K in the NVT ensemble. A first equilibration run of 1 ps was done using the Berendsen thermostat⁵⁷ with a coupling constant of 10.0 fs. The production time was 5 ps using the Nosé-Hoover chain thermostat,^{58,59} with a chain length of 3 and a coupling constant of 100.0 fs. The chosen timestep was 0.25 fs for both equilibration and production runs. The center of mass was kept fixed in order to avoid drifts.

3.4 Modifications included in the Force Field.

Some modifications were included in the force field published by Dwyer et al.²³ in order to reproduce the quantum-optimized geometries. The modified parameters correspond to four equilibrium bond lengths and an equilibrium bond angle, as it is shown in Figure 3.2. The modified parameters correspond to the central region that is most affected by the substitution of the cation.

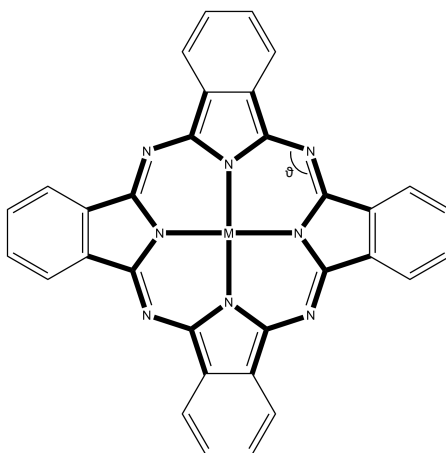


Figure 3.2: Modified geometric parameters.

Table 3.2: Modifications included in the equilibrium parameters.

Term	Original FF ²³	FePc	NiPc	CuPc	ZnPc
$b_{0(\text{Cu-N1})}$ (Å)	1.9400	1.9220	1.8369	1.9359	2.0060
$b_{0(\text{N1-C1})}$ (Å)	1.3847	1.3840	1.3780	1.3810	1.3830
$b_{0(\text{N2-C1})}$ (Å)	1.3310	1.3476	1.3435	1.3450	1.3460
$b_{0(\text{C1-C2})}$ (Å)	1.4592	1.4500	1.4505	1.4525	1.4535
$\theta_{0(\text{C1-N2-C1})}$ (°)	125.3075	120.3075	119.3075	120.3075	120.3075

In addition, the charges corresponding to the metal and the nearest nitrogen atoms are changed when the central atom is replaced by another $3d$ transition metal. To do so, the total charge of $\text{M}+4\text{N}$ remains in -1.719 , as schematized in Figure 3.3, but a redistribution of charge density is done. Keeping this value in all MPcs avoids the need of reassigning charges to the outer atoms of the complex. For this aim, the MKUFF charges obtained from the MP2 calculation are used. The q_M/q_{Zn} ratio (with $\text{M}=\text{Fe}, \text{Ni}, \text{Cu}$) is computed and then applied to the charge of the central metal. The charge of nitrogens is then calculated as a difference between the total charge of the region (-1.719) minus the metal charge, and divided by 4.

Table 3.3: Charges modifications included in the force field for the central MN_4 unit.

Charge	Original FF ²³	FePc	NiPc	CuPc
M	1.01500	0.89000	0.57480	0.77260
N1	-0.68350	-0.65240	-0.57360	-0.62305

3.5 EXAFS Spectrum Computation

Theoretical EXAFS spectra of the K-edge of metal-phthalocyanines have been computed using a set of snapshots extracted from both MD simulations, classical and Born-Oppenheimer. 500 evenly-spaced configurations were extracted from the trajectory to assure the convergence.

The global EXAFS spectrum, $\chi(k)$, is computed averaging all the individual spectra ob-

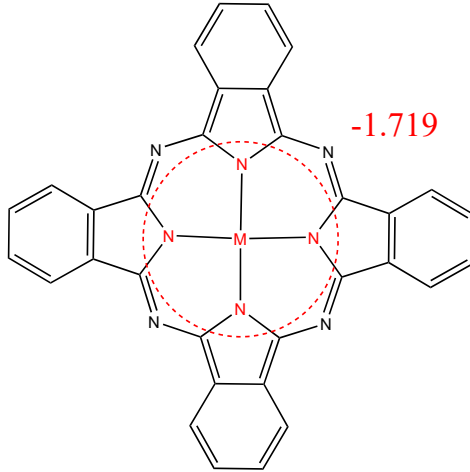


Figure 3.3: In red, the part of the complex in which the charges are modified. This region should remain with a charge of -1.719 after modifications.

tained for each snapshot:

$$\bar{\chi}(k) = \frac{1}{N_s} \sum_i^{N_s} \chi_i(k) \quad (3.1)$$

where $\chi_i(k)$ is the individual spectrum of each snapshot and N_s is the total number of them.

Following this strategy, the classical EXAFS equation can be modified according to the expression:

$$\chi(k) = \frac{1}{N_s} \sum_l^{N_s} \sum_{j'}^{paths} \frac{N_j'}{kR_{lj'}^2} S_0^2 F_j^{eff}(k) e^{\frac{-2R_{lj'}}{\lambda(k)}} \sin(2kR_j + \varphi_j(k)) \quad (3.2)$$

where N_s is the number of snapshots, index l identifies each of them and j' runs over all the scattering paths considered in every structure. In equation 3.2 the structural disorder arises from the summation over all spectra of different structures instead of using a model structure with associated Debye Waller factors ($e^{\frac{-2R_{lj'}}{\lambda(k)}}$).

EXAFS calculations for every snapshot were performed with the FEFF code (version 9.6).⁶⁰ The Hedin-Lundqvist potential was used to compute the electron density distribution within a self-consistent-field (SCF) approach. Hydrogen atoms were included to calculate the potential, but they were not included as backscatterers.⁶¹⁻⁶⁴ After studying the convergence, the cutoff radius around the absorber atom was set to 6 Å and the multiple scattering paths were extended up to 6 legs. ΔE_0 and S_0^2 applied were chosen for each

MPc to match the most intense oscillation of the experimental EXAFS spectrum. The k range employed was $\Delta k = 2.0\text{-}13.0 \text{ \AA}^{-1}$ and all the spectra were k^3 weighted.

Table 3.4: Parameters used for each metal in the EXAFS spectra computation.

	FePc	NiPc	CuPc (80 K)	CuPc (300 K)	ZnPc
MD					
E_0 (eV)	-5.5	-0.2	-2.5	-9.0	-8.0
S_0^2	0.7	0.75	0.85	1.0	1.0
BOMD					
E_0 (eV)	-5.5	-1.0	-2.5	-9.0	-8.0
S_0^2	0.7	0.75	0.8	1.0	1.0

CHAPTER 4

Results

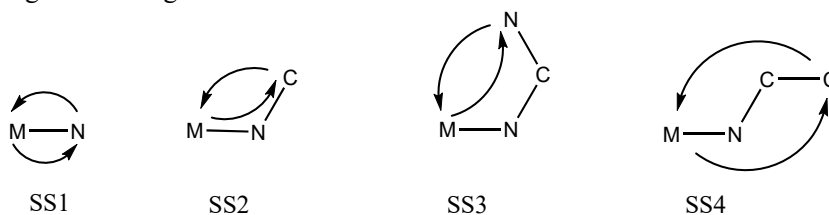
4.1 Previous experimental results

In the present study, theoretical results are compared with the published experimental EXAFS spectra. The experimental information, as well as the details of the fittings, were extracted from the works of Hong et al.,¹⁷ Rossi et al.¹⁶ and Carrera et al.¹⁵ Both studies agree that the EXAFS spectrum of metal-phthalocyanines is well described using only backscattering paths involving a single molecule. Paths involving other MPc molecules or solvent molecules are found to have negligible contributions compared to those involving intramolecular atoms.¹⁵ The considered backscattering paths employed in the experimental fittings are illustrated in Figure 4.1

The difficulty of the experimental fitting comes out when Carrera et al. considered the SS1-SS4, MS1-MS3 and MS5-MS8 paths in their fitting, while Rossi et al. took into account paths SS1-SS4 and MS1, MS2, MS4, MS5, MS7 and MS8. Furthermore, Hong et al. only considered two single scattering paths, SS1 and SS2. That is, there are discrepancies among the authors about the more relevant paths to be used in the fitting of the EXAFS spectra.

Regarding the calculation of the DW factors, each path has associated its own DW factor. In principle, it would be necessary to fit all of them, considering a large number of parameters -highly correlated- for each backscattering path. To simplify the problem, it is common to relate MS DW factors with those of SS according to the so-called *independent vibration model*.^{65,66} According to it, the fittings are performed with the following

Single Scattering Paths



Multiple Scattering Paths

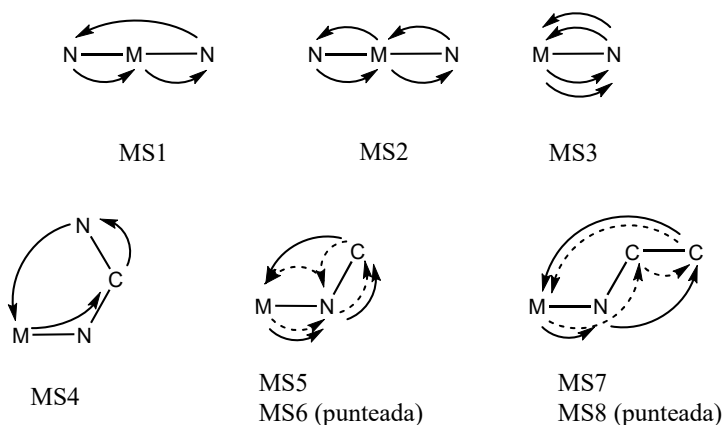


Figure 4.1: Backscattering paths, where M is the absorber atom.

considerations to reduce the number of free parameters:

$$\sigma_{MS1}^2 = \sigma_{MS2}^2 = 2\sigma_{SS1}^2 \quad (4.1a)$$

$$\sigma_{MS3}^2 = 4\sigma_{SS1}^2 \quad (4.1b)$$

$$\sigma_{MS7}^2 = \sigma_{SS4}^2 \quad (4.1c)$$

where the eq. 4.1c is introduced by Rossi et al. despite the fact that this is derived for the cases in which the atoms are aligned, that is, with an angle of 180° , while in the MS7 path the angle M-N-C is in the range 161° - 163° .

Table 4.1: Distances and DW factors obtained from the experimental fittings.

Path	FePc 80 K ¹⁶		NiPc 300 K ¹⁷		CuPc 80 K ¹⁶		CuPc 300 K ¹⁵		ZnPc 80 K ¹⁶	
	R (Å)	$\sigma^2 \cdot 10^3(\text{Å}^2)$	R (Å)	$\sigma^2 \cdot 10^3(\text{Å}^2)$	R (Å)	$\sigma^2 \cdot 10^3(\text{Å}^2)$	R (Å)	$\sigma^2 \cdot 10^3(\text{Å}^2)$	R(Å)	$\sigma^2 \cdot 10^3(\text{Å}^2)$
SS1	1.9325±0.0073	5.8	1.90±0.02	4	1.945 ± 0.006	3.06	1.95 ± 0.01	0.8	2.0023±0.0079	6.1
SS2	2.968 ±0.011	5.6	2.90±0.09	7	2.973 ± 0.009	2.5	2.97 ± 0.02	2	3.029 ± 0.012	6.0
SS3	3.378 ±0.013	5.4	3.29±0.03	1	3.38 ± 0.01	2.8	3.37 ± 0.02	4	3.418 ± 0.014	8.4
SS4	4.203 ±0.016	9.4	4.31±0.06	1	4.22 ± 0.01	6.3	4.1 ± 0.1	7	4.275 ± 0.017	7.8
MS1		11.6				6.12				12.2
MS2		11.6				6.12				12.2
MS3								3.2		
MS4		1.4				0				3.1
MS5		1.3				0		16		2.8
MS6								16		
MS7		9.4				6.30		10		7.8
MS8		26				33		10		17

The results of the experimental fits are illustrated in Table 4.1. At first sight, it is surprising that some single backscattering paths DW factors (SS1 and SS2) at 80 K are larger than at 300 K, where thermal agitation is higher. Also, in some cases there are fitted DW factors whose value is 0, as is the case for MS4 and MS5 paths for CuPc at 80 K. This makes no sense since the DW factor for SS paths that involves second and third coordination shells are different from 0, so the same is expected for the MS paths that involves the second and the third coordination shells. This issue will be discussed later.

4.2 Molecular Dynamics simulations results

4.2.1 Average structures from MD simulations: Testing the original Force Field

Table 4.2 collects the average distances, obtained from the MD simulations at 80 K, from the central zinc atom to the different coordination shells. The force field used is the one published by Dwyer et al.,²³ which from now on will be labeled as “original FF”. Those results are compared with the experimental ones, obtained from the fitting of EXAFS spectrum reported by Rossi et al.,¹⁶ and from the QM optimization at MP2 level.

Table 4.2: Average distances for the first four shells of ZnPc from MD simulations, from experimental EXAFS fitting and from MP2 optimization. R_n , with $n = 1, 2, 3, 4$, are the distances of the metal to the 1st, 2nd, 3rd and 4th coordination shells, represented in Figure 3.1.

	Original FF ²³	Experimental ¹⁶	MP2	Modified FF
R_1 (Å)	1.947	2.0023 ± 0.0079	1.9850	1.985
R_2 (Å)	2.970	3.029 ± 0.012	2.9968	2.996
R_3 (Å)	3.339	3.418 ± 0.014	3.3902	3.390
R_4 (Å)	4.220	4.275 ± 0.017	4.2400	4.241

Differences between the original FF and the experimental results are typically about 0.05 Å. In Figure 4.2 the average theoretical EXAFS spectrum based on the original FF simulation has been represented to check if it reproduces the main features of the experimental one. Despite its complexity, we see that the oscillations of the experimental spectrum and its positions are largely reproduced. Nonetheless, in spite of the overall good reproduc-

tion, there are regions that can be improved.

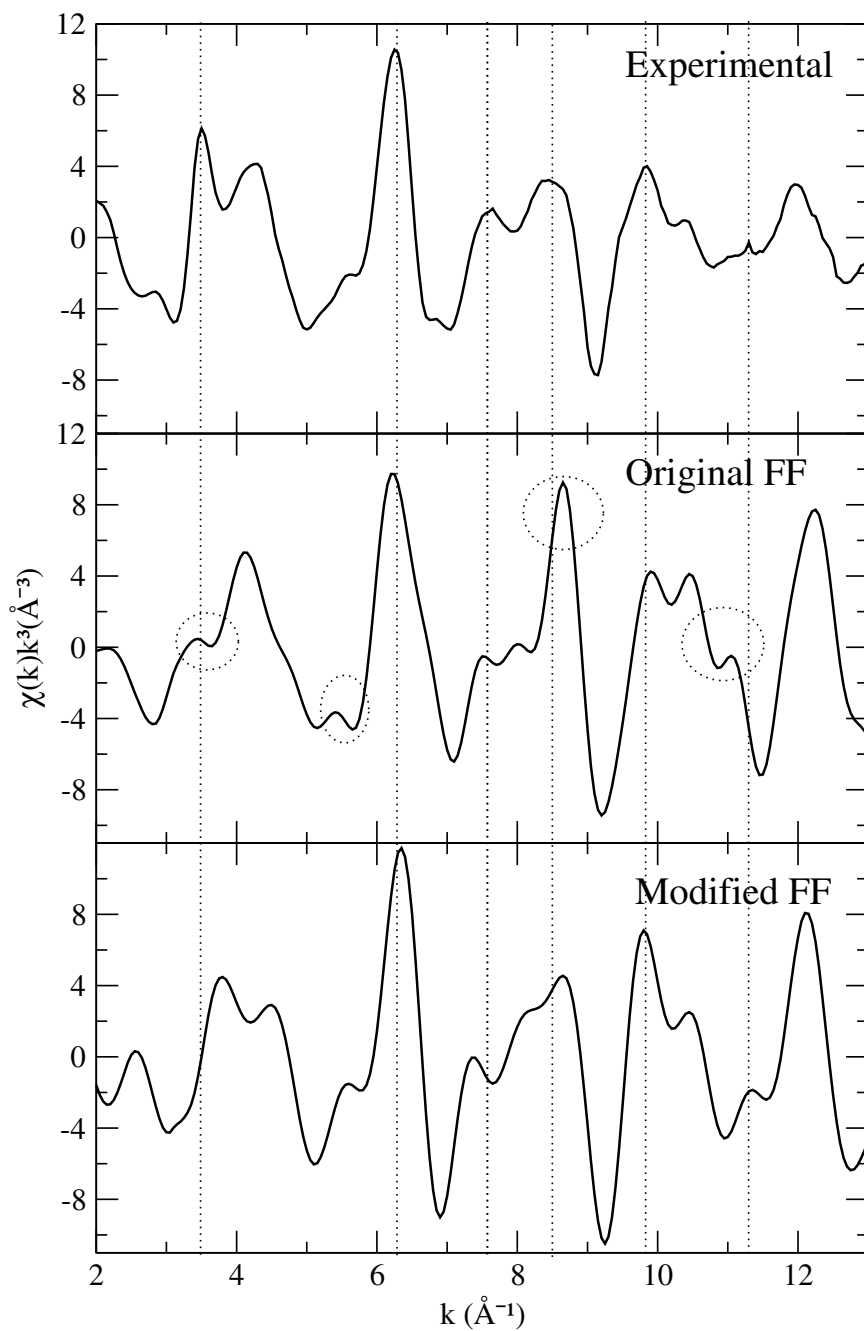


Figure 4.2: ZnPc EXAFS spectra. On top, the experimental one published by Rossi et al.,¹⁶ in the middle, the average EXAFS spectrum obtained from the original FF,²³ and at the bottom, the average EXAFS spectrum obtained from the modified FF. The dotted vertical lines serve as a visual aid to facilitate comparisons.

The origin of these discrepancies can be twofold: on the one hand, the structural dif-

ferences observed in Table 4.2 are significant enough to show up in the comparison of the spectra and, on the other hand, there are significant deviations produced by the DW factors associated with each of the contributions. Therefore, with the aim of improving the reproduction of the experimental spectra, the original force field has been modified. To change the DW factors, it would be necessary to modify the effective force constants acting between bonded atoms, which is an involved task in the case of such a complicated system. Consequently, only some equilibrium distances have been modified in some of the terms corresponding to the bond-stretching contribution and one of the angles, in order to reduce the discrepancies present in Table 4.2, as described in section 3.4. This new force field is called “modified FF”. The modifications introduced were illustrated in Table 3.2. Last column of Table 4.2 collects the average distances obtained from the modified FF simulations.

MD simulations with the modified FF yield structural results in which the theoretical-experimental agreement is clearly improved. The lower part of Figure 4.2 shows the spectra obtained after the modifications made in the original FF. It is evident that the average spectra obtained from the modified FF improves most of the deficiencies observed in the case of the original one. The main differences are highlighted with dotted ellipsoids.

The different frequencies contributing to $\chi(k)$ depend on the path lengths, and therefore, on distances between the backscatterers, as can be seen in Eq. 2.15. In turn, in this case the rigidity of the molecule makes relevant a multitude of contributions with different frequencies, what defines a very complex spectrum. That is the reason why small structural modifications, such as those introduced in Table 3.2, give rise to significant changes in the spectrum, due to interference phenomena. In a more labile system, this effect would be much less intense.

4.2.2 Extension to other transition-metal phthalocyanines

Due to the clear improvement obtained in the previous section with the modification of the FF published by Dwyer et al.,²³ we propose the extrapolation of this methodology to other transition metal phthalocyanine complexes. Those metals are Fe, Ni and Cu, since they belong to the same transition series and their experimental EXAFS spectra are available.

In Table 4.3 we present the average distances obtained for the MD simulations, the ex-

perimental ones and the QM-optimized geometries at MP2 level corresponding to the 4 MPcs studied. The BOMD results are also summarized, but they will be discussed in the next section.

Table 4.3: Average distances for the first four shells of MPc from MD and BOMD simulations, experimental results from EXAFS fitting and MP2 optimizations.

FePc (80 K)	MD	BOMD	Experimental ¹⁶	MP2
R_1 (Å)	1.936	1.933	1.9325	1.936
R_2 (Å)	2.967	2.975	2.968	2.966
R_3 (Å)	3.377	3.381	3.378	3.377
R_4 (Å)	4.207	4.209	4.203	4.207
NiPc (300 K)	MD	BOMD	Experimental ¹⁷	MP2
R_1 (Å)	1.888	1.899	1.90	1.888
R_2 (Å)	2.934	2.944	2.90	2.934
R_3 (Å)	3.364	3.361	3.29	3.363
R_4 (Å)	4.173	4.179	4.31	4.174
CuPc (80 K)	MD	BOMD	Experimental ¹⁶	MP2
R_1 (Å)	1.946	1.959	1.945	1.946
R_2 (Å)	2.972	2.985	2.973	2.971
R_3 (Å)	3.379	3.386	3.38	3.379
R_4 (Å)	4.214	4.225	4.22	4.213
CuPc (300 K)	MD	BOMD	Experimental ¹⁵	MP2
R_1 (Å)	1.946	1.959	1.95	1.946
R_2 (Å)	2.972	2.983	2.97	2.971
R_3 (Å)	3.379	3.382	3.37	3.379
R_4 (Å)	4.214	4.222	4.1	4.213
ZnPc (80 K)	MD	BOMD	Experimental ¹⁶	MP2
R_1 (Å)	1.985	1.996	2.0023	1.985
R_2 (Å)	2.996	3.011	3.029	2.997
R_3 (Å)	3.390	3.396	3.418	3.390
R_4 (Å)	4.241	4.252	4.275	4.240

On one hand, MP2 distances are quite close to those provided by the experimental EXAFS fittings. On the other hand, it can be seen that the average distance of the first 4 shells for the classical MD fully reproduces the results of the quantum optimizations, as intended.

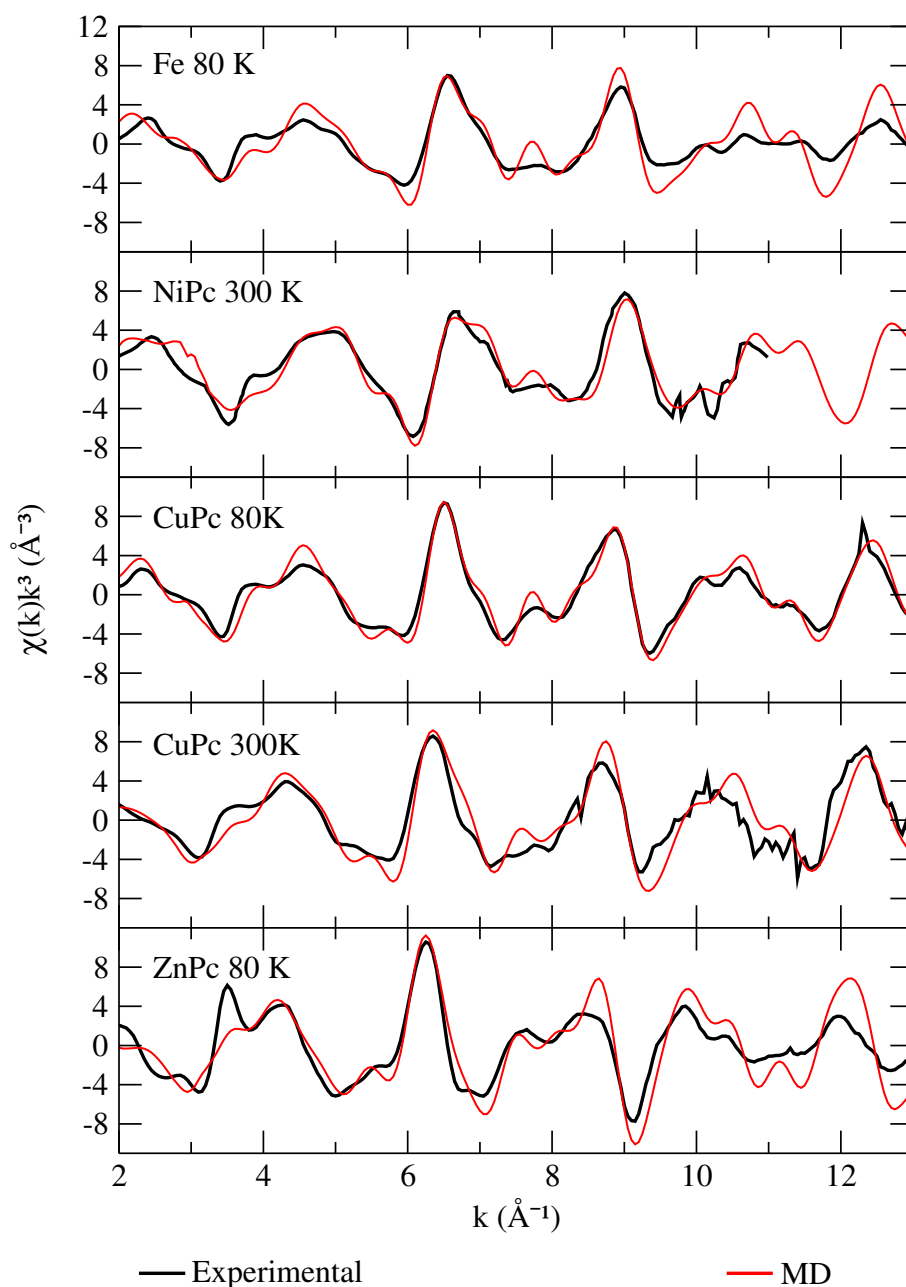


Figure 4.3: Theoretical (classical MD) and experimental EXAFS spectra.

In Figure 4.3 are compared the theoretical spectra extracted from classical MD simulations with the experimental ones. We can see that there is an excellent reproduction of

the experimental spectra main features and its positions, specially in the case of NiPc and CuPc at both temperatures, 80 K and 300 K. It is worth mentioning that the amplitude of the theoretical spectra of FePc and ZnPc at high k values is clearly larger than the experimental one, which do not occur in the rest of the species. In the case of FePc, if the experimental spectrum is compared with the experimental spectra of the other MPcs, it is observed that its amplitude is significantly lower at high k values. In the works of Kim et al.⁶⁷ and Choi et al.,⁶⁸ EXAFS spectra of iron (II) phthalocyanines were recorded, obtaining a slightly higher amplitude at high k than compared to the one reported by Rossi et al.

The contributions and the amplitude of the total spectra will be discussed in the following sections.

4.3 Born-Oppenheimer Molecular Dynamics simulations results

The advantage of BOMD simulations over classic MD simulations is that they do not need to use any force field. After checking that the quality of the level of theory used for BOMD is comparable to the MP2 results (section 3.1), we can use the quantum results as a double check for the quality of our force fields.

The differences in shell distances, reported in Table 4.3, between classical MD and BOMD are typically in the hundredth of Å. To see if there are significant differences in the average EXAFS spectra from classical MD and BOMD simulations, we plot them in Figure 4.4.

Although there are slight differences between the two theoretical spectra for each species, main spectral features are in the same positions and with very similar amplitudes. The largest coincidence in the shell distances between the classical MD and BOMD simulations is found in the FePc. In this case, both theoretical spectra exactly match. In the rest of MPcs, classical MD and BOMD simulations give slightly different spectra but they are not so relevant because they do not affect significantly the positions neither the amplitudes of the spectral features.

Therefore, the scanty differences between both theoretical spectra can be attributed, in

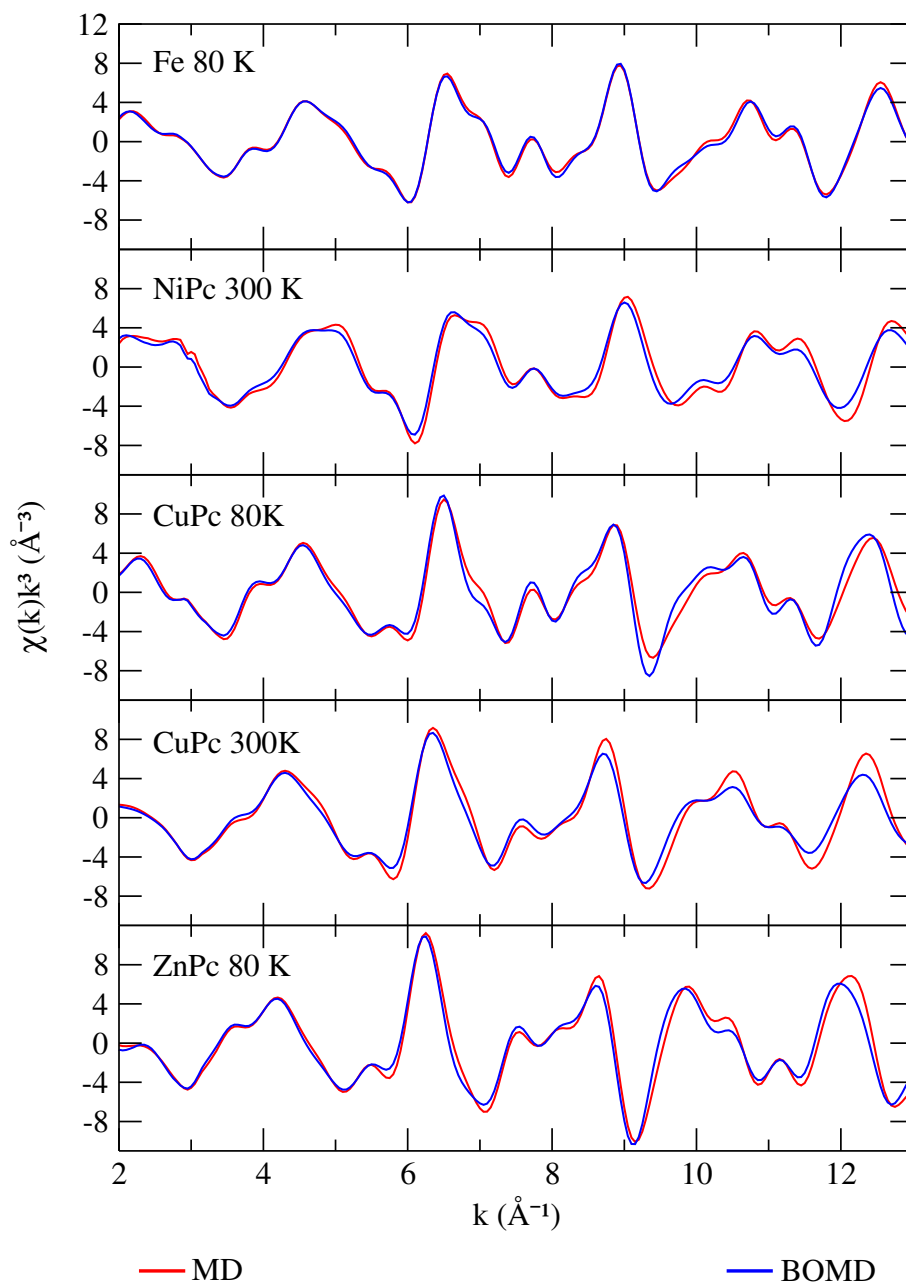


Figure 4.4: Theoretical (classical MD and BOMD) EXAFS spectra.

this case, either to the different DW factors obtained from each simulation type or to the different simulation times (5 ps vs 1 ns).

4.4 Analysis of the theoretical EXAFS spectra

4.4.1 Temporal convergence

Due to the high computational cost of BOMD simulations, we have a production time of only 5 ps. In contrast, classical molecular dynamics simulations are extremely cheap. With the help of classical MD simulation we can study the temporal convergence of the EXAFS spectra. In Figure 4.5 the average EXAFS spectra of MPCs are plotted. In red, the spectra extracted from 1 ns of simulation, and in turquoise, the spectra extracted from 5 ps of simulation. Both of them are computed with the same number of snapshots and with the same parameters (S_0^2, E_0). There is almost no difference between them. We can safely consider that 5 ps of simulation is enough to have a converged EXAFS spectrum, validating therefore the BOMD spectra already presented.

4.4.2 Convergence of the theoretical spectra with the number of shells and legs

Figure 4.6 shows the evolution of the average spectrum of ZnPc with the increase of the number of shells around the absorber atom and with the number of legs of the scattering paths. The analysis is done for Zn and we assume results can be extrapolated to the rest of the complexes.

In the generation of the spectra by shells, the number of legs were enough so that this parameter does not influence the analysis. Convergence is reached when a total of 5 shells around the absorbing atom are considered.

The right part of the same figure shows the evolution of the oscillations in the spectrum when considering backscattering paths with an increasing number of legs. Comparably to the analysis by shells, in this case a sufficient number of shells around the absorbing atom have been considered so that this parameter does not interfere in the analysis of the number of legs. In this case, convergence is achieved by considering paths up to 6 legs.

The evolution of both sets of spectra does not show a clear pattern, reflecting complex contributions when gradually increasing each of the parameters analyzed. It is interesting to note the simplicity of the wave $\chi(k)$ when considering only the first shell, defined by

CHARMM

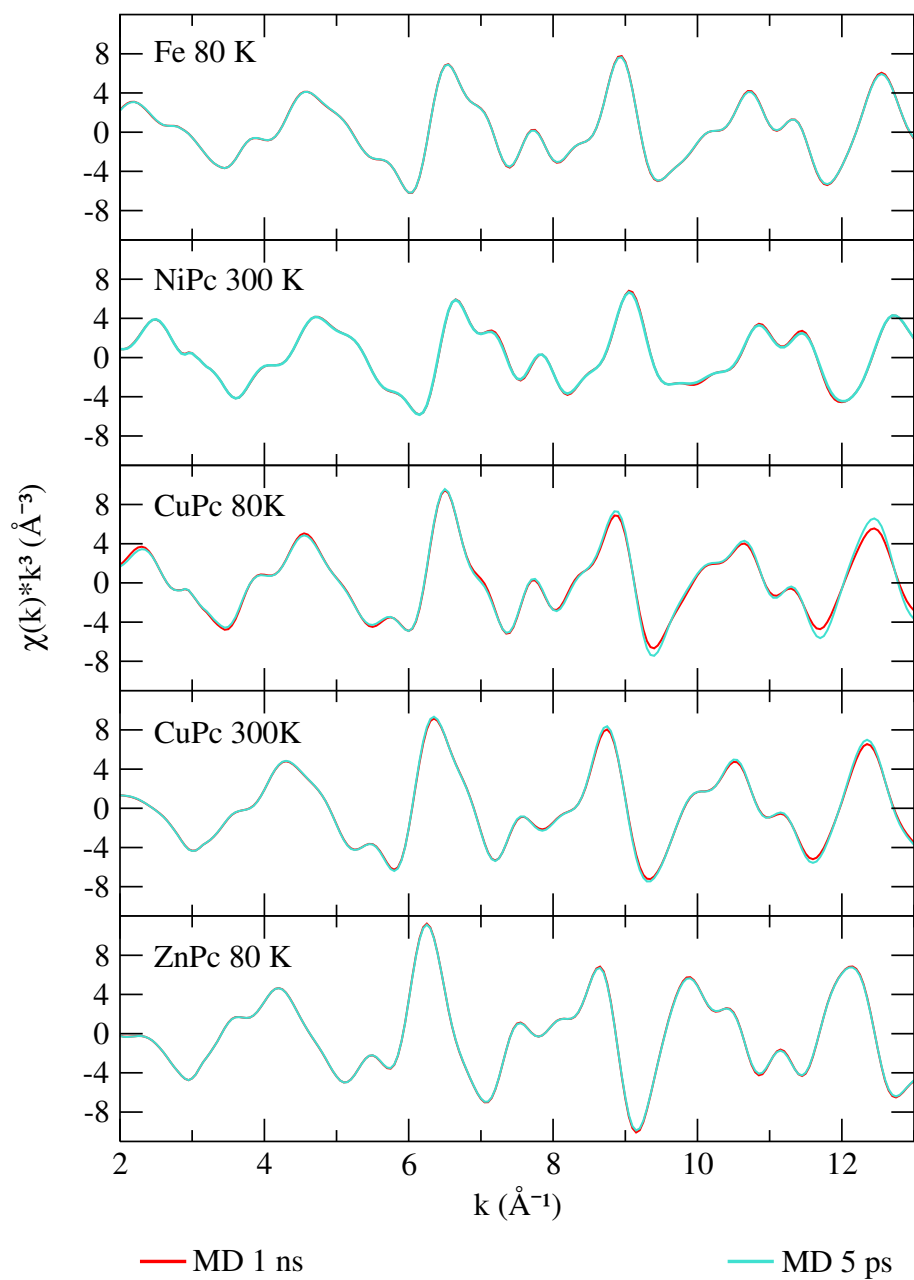


Figure 4.5: Theoretical average EXAFS spectra computed for 5 ps and 1 ns of simulation.

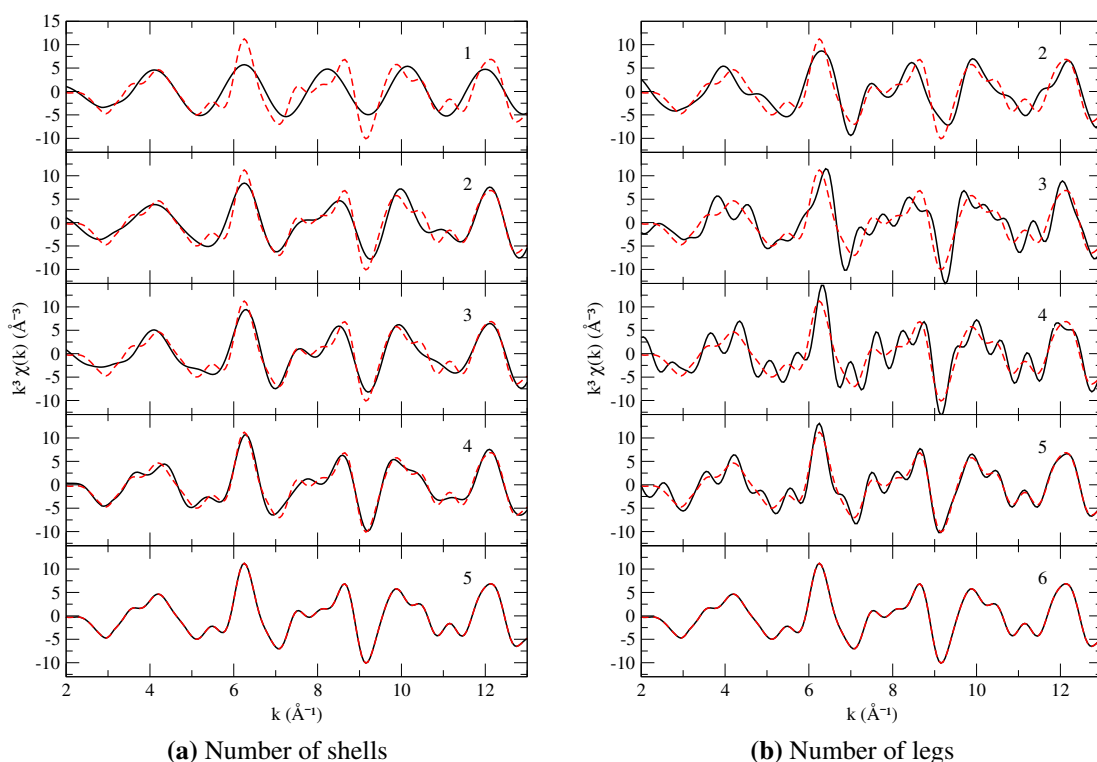


Figure 4.6: Evolution of the average ZnPc spectra at 80 K as the number of shells (a) and the number of legs (b) increase. The final converged spectrum is shown in dashed line to facilitate comparison.

the four nitrogen atoms bonded to the metal. In this case, the predominant contribution of the simple Zn-N backscattering path does not account for the shape of the spectrum. In contrast, the first spectrum in Figure 4.6b, in which only the single scattering paths are considered, already presents a structure far from simple, capturing to a large extent the global complexity of the spectrum. It is worth noting in this case that the pattern observed is the result of superimposing SS contributions corresponding to successive coordination shells around the central metal ion, each with significantly different distances.

The results presented are completely compatible with the conclusions presented by Carrera et al.¹⁵ and Rossi et al.¹⁶ in their respective studies. In the first case, Carrera et al., in their analysis of the Fourier transform of the EXAFS spectrum of CuPc at 300 K, confirms that the signal beyond 4 Å is still intense enough to require the inclusion of the fifth (5.5 Å) and sixth (6.5 Å) shells in the analysis. However, taking into account these shells in the experimental analysis would mean a large increase in the number of parameters to fit,

since 42 new MS paths would appear with an intensity greater than 10%,¹⁵ making fitting non feasible. Rossi et al. come to a similar conclusion, but in this case analyzing XANES spectra instead of EXAFS. According to them, 6 shells would be necessary to grasp all the features observed in the experimental spectra.

4.4.3 Model structure concept

One option at this point is to compare the “complete” average theoretical spectra with the spectra calculated taking into account only the paths included in the fittings of experimental spectra. However, before addressing this issue, an interesting question within the fitting process of an experimental spectrum will be considered. In the fitting of experimental spectra a model structure is adopted which essentially determines the contributions to the final spectrum. As already mentioned, the fitting of the spectra provides, basically, the distance of the backscattering atoms and the static and dynamic disorder that they exhibit. This disorder is reflected in the Debye-Waller factor associated with each group of backscattering paths.

With the available structural information we can answer the following question: Is an average spectrum, taking into account only certain backscattering paths, equivalent to generating a single spectrum based on a model structure, considering the same paths, and including the extracted DW factors from the simulation? In the first case, the average spectrum is built from the structures extracted from the MD simulations, incorporating in each of them only the set of selected backscattering paths. In the second case, a single spectrum is generated on the basis of a model structure, also selecting the same paths as in the first case, and introducing the disorder through the DW factors resulting from the MD simulations. In other words, we are asking about the equivalence of expressions 2.15 and 3.2.

Figure 4.7 answers the question proposed. It compares the spectrum obtained from the statistical average of individual spectra incorporating only the backscattering paths used in the experimental study of Rossi et al. and the single spectrum obtained by selecting the same paths for the average structure of the simulation and with the DW factors obtained theoretically. Modified FF at 80 K for ZnPc is chosen as test case. Equivalent results must be expected for the other metal phthalocyanines.

It is interesting to see how the same results can be reproduced from a single spectrum, without the need to generate a spectrum for each snapshot of the MD trajectory. This strategy entails lower computational cost and considerably less time, although the *a priori* knowledge of the main contributions (paths) become compulsory. It should be noted that the intrinsic rigidity of the studied system greatly favors the equivalence between both strategies. It would be interesting to do this comparison in coordination environments with a greater degree of flexibility or in more disordered systems.

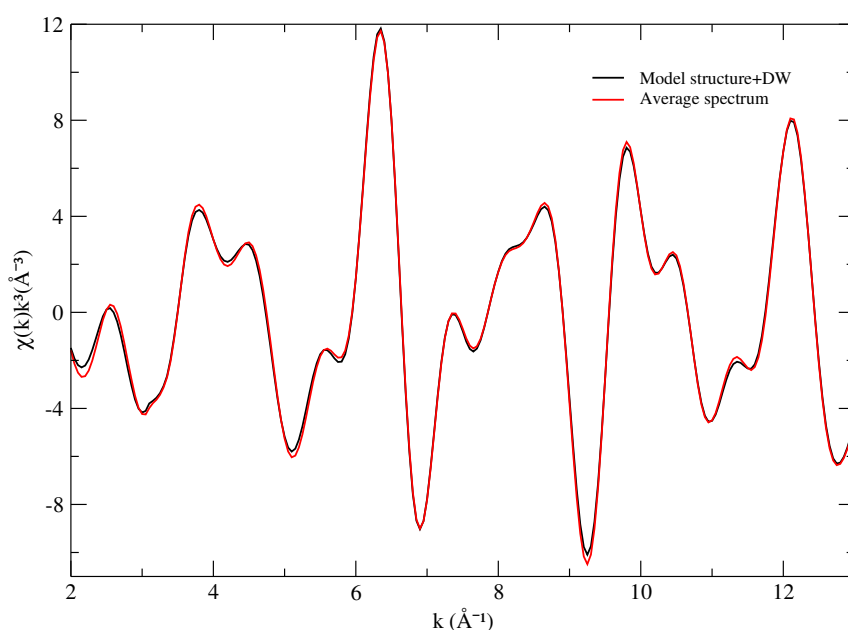


Figure 4.7: Average EXAFS spectrum (in red) obtained from ZnPc MD simulation at 80 K including only the scattering paths considered by Rossi et al.¹⁶ In black, EXAFS spectrum obtained for the average structure from the simulation considering the same paths whose DW factors are extracted from the same simulation.

4.5 A comparison between Debye-Waller factors

4.5.1 Results from MD simulations

The complexity of fitting the EXAFS spectra of the MPCs has its origin in its high molecular rigidity, which makes it necessary to take into account a large number of contributions.

This complicates the fitting of the Debye-Waller factors associated with each backscattering path, since they are strongly correlated with other parameters that affect amplitude.

Due to the exponential character of the term that contains the Debye-Waller factor in the EXAFS equation, the precision in its determination is crucial for making a quantitative analysis of the spectrum. In fact, its determination it is a limiting factor when making structural characterizations, since it affects the amplitude of the signal, related, for example, to the coordination number around the absorbing atom. In our system, that parameter is known, but this is not the case in many other systems with ligands that have low residence times in the environment of the absorber. In addition, it is strongly correlated with the amplitude reduction factor S_0^2 , so its theoretical estimation supposes a great improvement in the fitting and in the reduction of the number of free parameters needed to carry out the fitting.

The strategy that followed the experimental studies of Rossi et al.¹⁶ and Carrera et al.¹⁵ was to relate some of the DW factors of the MS paths with those of SS through simple formulas, as discussed in the Methodology section. These approximations imply a reduction in the number of free parameters to fit. However, both studies differ in the selection of backscattering paths, as well as in some of the expressions that relate the DW factors of the different contributions. Those facts simply illustrates the complexity of the analysis.

The aim of this section is to discuss the results of the experimental fittings and see how they compare with our theoretical results.

We can calculate directly the DW factor for every scattering path in our simulation. For the aim of comparison, we have computed the DW factors of the scattering paths that experimentalists employed in the fitting process, schematized in Figure 4.1. Figure 4.8 shows the theoretical and the experimentally fitted DW factors. First, we can see that the differences between the DW factors of MD simulations and those of the experimental fitting can be as high as one order of magnitude. Also, in some cases there are fitted DW factors whose value is 0, as is the case for MS4 and MS5 paths for CuPc at 80 K, as stated in a previous section. This shows some degree of inconsistency in the analysis of the experimental spectra.

When comparing both MD simulations, classical and Born-Oppenheimer, we can see that the differences are smaller and that they follow the same trend. The values are sum-

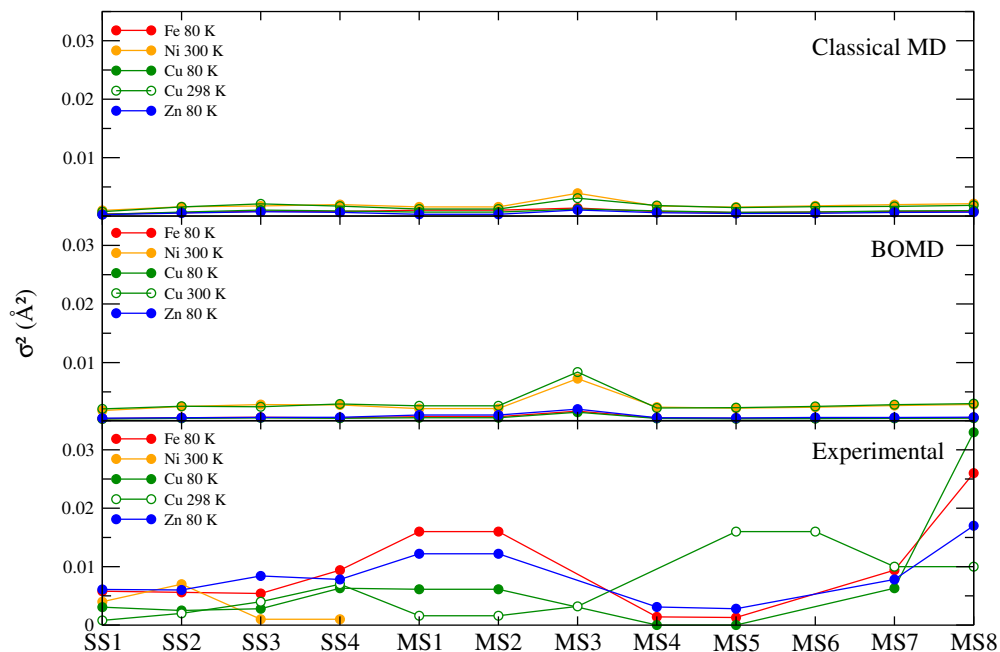


Figure 4.8: Debye-Waller factors calculated for the classical MD and BOMD and its comparison with the fitted experimental values.

marized in Table 4.4. The maximum value of the ratio $\sigma_{BOMD}^2/\sigma_{MD}^2$ when comparing classical MD and BOMD for the same complex is less than 2, thus, all the values are in the same order of magnitude. Even though there are differences between the values of the DW factors of both theoretical simulations, these are not reflected in the average EXAFS spectra, because there are so many contributions to the total simulated spectra that the differences are diluted.

Table 4.4: DW factors of MD simulations multiplied by a factor 10^3 . Units are \AA^2 .

Sys.	FePc 80 K		NiPc 300 K		CuPc 80 K		CuPc 300 K		ZnPc 80 K	
	MD	BOMD	MD	BOMD	MD	BOMD	MD	BOMD	MD	BOMD
SS1	0.346	0.428	0.977	1.82	0.303	0.384	0.768	2.10	0.262	0.514
SS2	0.600	0.581	1.60	2.50	0.692	0.490	1.57	2.55	0.521	0.590
SS3	0.835	0.664	1.74	2.83	1.04	0.562	2.09	2.46	0.745	0.656
SS4	0.799	0.577	1.99	2.77	0.891	0.494	1.71	2.93	0.650	0.658
MS1	1.02	0.774	1.57	2.15	0.688	0.589	1.21	2.62	0.312	1.05
MS2	1.02	0.774	1.57	2.16	0.688	0.591	1.21	2.62	0.312	1.05
MS3	1.39	1.71	3.91	7.26	1.21	1.54	3.07	8.38	1.05	2.06
MS4	0.774	0.549	1.72	2.40	0.901	0.462	1.81	2.25	0.592	0.590
MS5	0.611	0.470	1.55	2.22	0.646	0.407	1.45	2.31	0.449	0.556
MS6	0.693	0.488	1.76	2.38	0.710	0.443	1.62	2.51	0.473	0.633
MS7	0.796	0.547	1.96	2.67	0.880	0.482	1.67	2.82	0.628	0.640
MS8	0.847	0.616	2.13	2.84	0.951	0.508	1.85	2.99	0.681	0.678

As it was said, the DW factor accounts for the disorder around the absorber atom. We can visualize the trajectories that follow the atoms in both kinds of MD simulations. In Figures 4.10 and 4.11 are represented the trajectory of ZnPc atoms in the classical MD and BOMD simulations, respectively. For both cases, it is observed that the oscillations of the atoms are much larger in the axis perpendicular to the molecular plane. In addition, their trajectories follow a "banana" shape, schematized in Figure 4.9, specially appreciable in the BOMD trajectory. Thus, the absorber-backscatter distances do not change noticeably because they follow paths close to an arc of a circle. This motion is not reflected in the DW factors, which account for the differences in the radial distance from the absorber to the backscatter atoms.

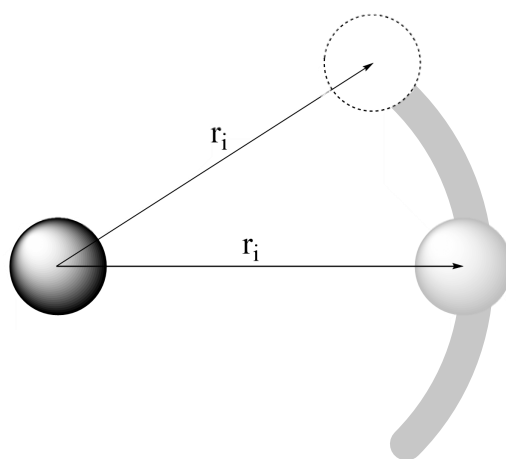


Figure 4.9: Representation of the backscatter atom movement following a "banana shape". Shaded line represents the radial amplitude of the motion.

We can see this phenomenon through numbers. In Figure 4.12 we plot the calculated square of the standard deviations around the average position for all the atoms in the three components for ZnPc simulations (both classical MD and BOMD). The molecule is in the xy plane. The square of the standard deviation is more than 10 times larger for the z axis contribution than for the x or y ones. This fact stands out especially in the case of BOMD, where the deformations increase considerably in the farthest shells. The value of the square of the standard deviation for the total distance r (DW factor in single scattering paths) is closer to the deviations in the x and y axes. Thus, the oscillations that do not change significantly the absorber-backscatter distance are not reflected in the DW factors. The result is equivalent for the the rest of MPcs.

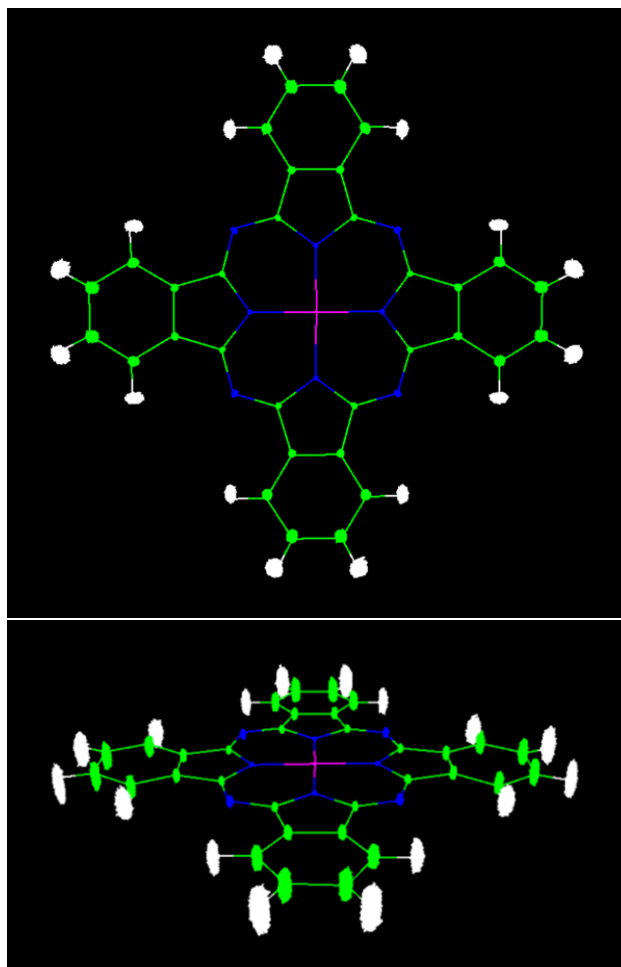


Figure 4.10: Representation of the trajectory followed by the atoms in the classical MD simulation of ZnPc at 80 K.

The underestimation of DW factors leads to exaggeration of the EXAFS signal, which we may be compensating for with small values of S_0^2 (Table 3.4). However for CuPc at 300 K and ZnPc at 80 K cases, the S_0^2 value used for the theoretical spectra is 1, so, despite having much smaller DW factors than those fitted experimentally, we get EXAFS spectra with the same amplitudes than the experimental ones. This fact can be again a proof of the effect of the interference pattern generated when all the scattering paths contributions are included in the generation of the EXAFS spectra. That is, the lack of scattering paths included in the fitting of the experimental information can be compensated with higher DW factors. In the case of FePc and ZnPc, as mentioned, we still have problems of higher amplitudes at high k values in the theoretical spectra despite of the fact that the amplitude of the spectra fit well at low k , either with the use of a small S_0^2 (FePc) or not (ZnPc).

There are unresolved issues concerning the amplitude of EXAFS spectra: it is not clear

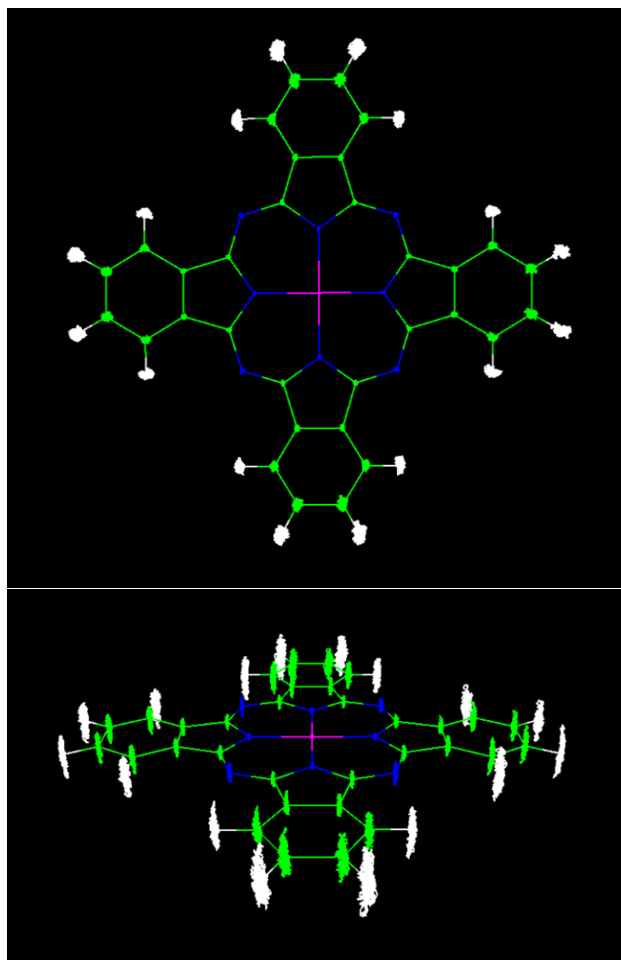


Figure 4.11: Representation of the trajectory followed by the atoms in the BOMD simulation of ZnPc at 80 K.

why in some cases the intensity matches the experimental ones and in others it does not. Factors like the extraction and analysis of the raw data, possible self-absorption problems,⁶⁹ etc, should be considered and analyzed.

4.5.2 Analyzing DW factors relationships applied in the experimental fittings

We can also check if the relationships between DW factors of SS and MS applied by the experimentalists (eq. 4.1) are supported by the simulation results. Table 4.5 collects the computed relationships for our simulations.

In order to apply the independent vibration model in the experimental fittings, two premises must be met: the thermal motion of the atoms in the direction perpendicular to the bond is small compared to the bond distance, and the movement is not correlated,³⁷ that is, the

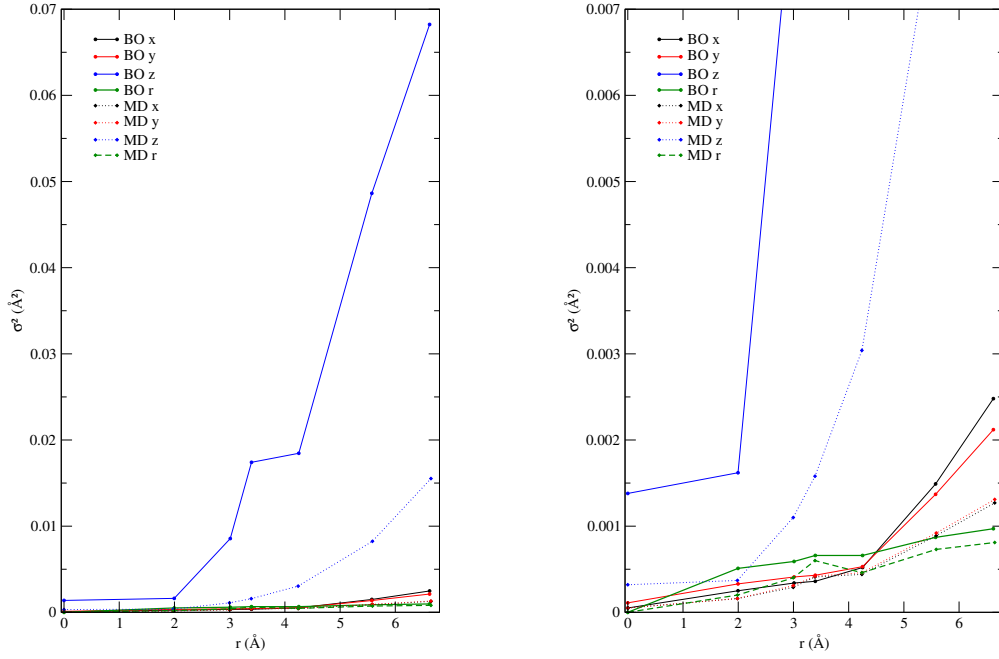


Figure 4.12: Representation of the square of the standard deviation around the average position for each shell for both classical and MD simulations. On the left, the whole graphic, on the right, a zoom $\times 10$ in the y axis.

Table 4.5: Calculation of the relationships between the theoretical Debye-Waller factors. The last row corresponds to the approximations imposed in the experimental fittings.

System		$\frac{\sigma_{MS1}^2}{\sigma_{SS1}^2}$	$\frac{\sigma_{MS2}^2}{\sigma_{SS1}^2}$	$\frac{\sigma_{MS3}^2}{\sigma_{SS1}^2}$	$\frac{\sigma_{MS7}^2}{\sigma_{SS4}^2}$
FePc 80 K	DM	2.94	2.94	4.00	1.00
	BOMD	1.81	1.81	4.00	0.95
NiPc 300 K	DM	1.61	1.61	4.00	0.99
	BOMD	1.68	1.68	4.00	0.96
CuPc 80 K	DM	2.27	2.27	4.00	0.99
	BOMD	1.53	1.54	4.00	0.97
CuPc 300 K	DM	1.58	1.58	4.00	0.97
	BOMD	1.25	1.25	4.00	0.96
ZnPc 80 K	DM	1.19	1.19	4.00	0.97
	BOMD	2.05	2.04	4.00	0.97
Imposed		2	2	4	1

oscillations of the atoms are not influenced by the oscillations of the other atoms.

First of all, classical MD and BOMD simulation results differ and do not follow a clear trend. We can observe that the first two relationships, which involve the paths MS1, MS2 and SS1, have a maximum error of almost the 50%. Those paths involves the central metal and the four-nearest nitrogen atoms. The origin of the discrepancies between the value expected from the independent vibrations model and the values extracted from simulations lead us to think that the independent vibrations model is not valid in the case of MS paths that involve the closest shells to the metal. It makes sense considering that phthalocyanine is a single tetradentate, aromatic (and therefore rigid) ligand. We can think that the movement of the nitrogens that bind the metal is correlated, since they are subject to the influence of the ring, which is a single entity. This theory is supported by the study of Z. Liu et al.⁷⁰ of the vibrational structure of MPcs. They affirm that all the normal modes above 955 cm⁻¹ mainly involve in plane bending (IPB) vibrations, and that is difficult for a bond to vibrate without involving other bonds for such a macrocyclic ring. Furthermore, IPB are the kind of vibrations that “appears” when calculating the DW factors, as mentioned before. However, the imposed ratios in the experimental analysis are very reasonable approximations.

In the last expression, which relates the paths MS7 and SS4, the equivalence is essentially fulfilled. The movement of the four different atoms that involves the MS7 paths may be decorrelated enough to fulfill the conditions needed to apply the independent vibrations model.

To understand why the relationship between MS3 and SS1 is exactly fulfilled for all the simulations of all the complexes, we have to go to the equation we use to calculate the DW factor. For the SS1 path it would be:

$$\sigma_{SS1}^2 \equiv \langle (\vec{r}_i - \vec{r}_0)^2 \rangle_i \quad (4.2)$$

Where \vec{r}_0 is the equilibrium distance from the absorbing atom to the backscatter, and \vec{r}_i is the instantaneous position of the backscatter atom, as illustrated in Figure 4.13. For the case of the MS3 path, σ_{MS3}^2 would be calculated as:

$$\sigma_{MS3}^2 \equiv \left\langle \left(\frac{\vec{r}_i - \vec{r}_0 + \vec{r}_i - \vec{r}_0 + \vec{r}_i - \vec{r}_0 + \vec{r}_i - \vec{r}_0}{2} \right)^2 \right\rangle_i = \left\langle \left(\frac{4\vec{r}_i - 4\vec{r}_0}{2} \right)^2 \right\rangle_i \equiv 4\sigma_{SS1}^2 \quad (4.3)$$

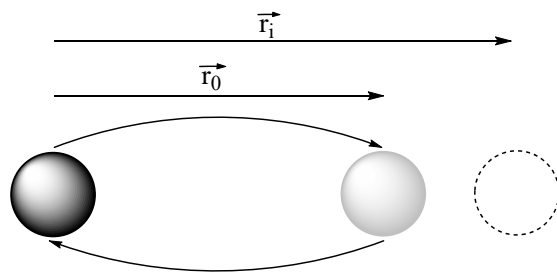


Figure 4.13: Single scattering path, indicating instantaneous, r_i , and equilibrium, r_0 , distances

Thus, by definition, $\sigma_{MS3}^2/\sigma_{SS1}^2$ is always fulfilled.

4.5.3 Average EXAFS spectra selecting paths

To shed light on the origin of the differences between the theoretical and experimental DW factors, average EXAFS spectra have been generated using only the paths that the experimentalists consider in their fits.

As a first result, Figure 4.14 shows the average spectra calculated from selecting, on the one hand, the paths used by Rossi et al. and those used by Carrera et al. Clearly there are no appreciable differences, so we can consider that the selection of paths is equivalent between both authors. From now on, we will make comparisons with the average spectrum generated with the paths selected by Rossi et al.

In Figure 4.15 we plot the total average spectra obtained from classical MD and BOMD simulations, and the average spectra selecting only the paths from the work of Rossi et al. for each simulation.

Although, for both classical MD and BOMD, some of the main features are present, such as the peaks at 6 \AA^{-1} and $8-9 \text{ \AA}^{-1}$, there are regions that remain incomplete. That is, the average spectra with the selected paths is not “converged”. In Figure 4.16 we plot the average EXAFS spectra only including the selected paths and the experimental ones. If we compare Figure 4.3 with Figure 4.16, the low k region gets considerably worse when going from the “total” spectrum to the spectrum generated selecting paths. In this region, MS paths are especially relevant. There are also appreciable differences in the region $7-9 \text{ \AA}^{-1}$. When we generate the theoretical EXAFS, for a symmetric structure, there are around 300 paths (not counting degeneracy) that contribute to the final spectrum. In the experimental fittings, however, the contribution of only 10-12 paths is taken into account.

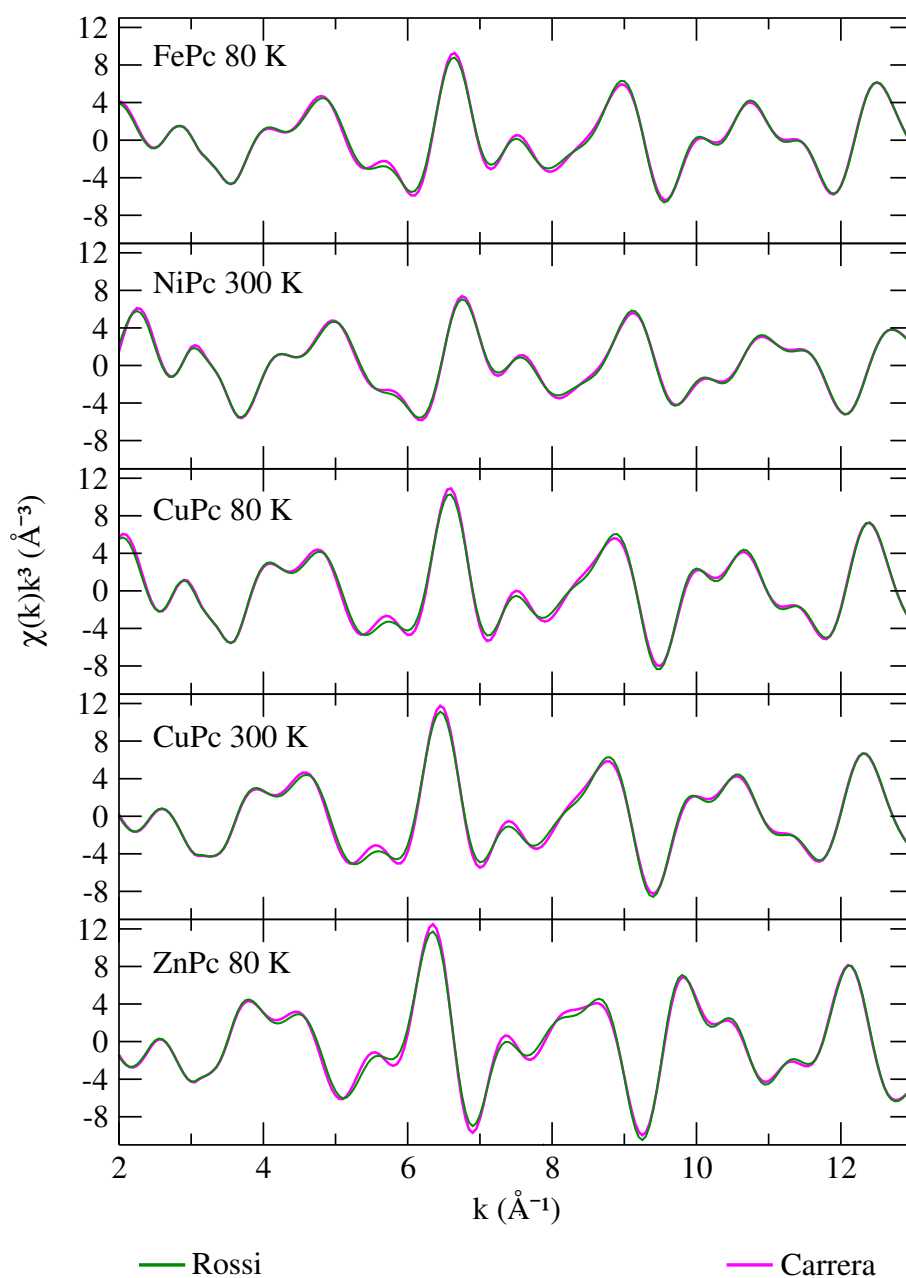


Figure 4.14: Comparison of the average EXAFS spectra using only the paths selected by the experimentalist for the spectra building. In green, the spectra resulting from the selection of the paths chosen by Rossi et al. In orange, the same but for the paths selected by Carrera et al.

The lack of paths considered in the fit may be compensated by larger DW factors, leading, at least partially, to the observed differences between the theoretical results and the experimental fits (Tables 4.1 and 4.4). It is important to note that 10-12 paths supposes, in this

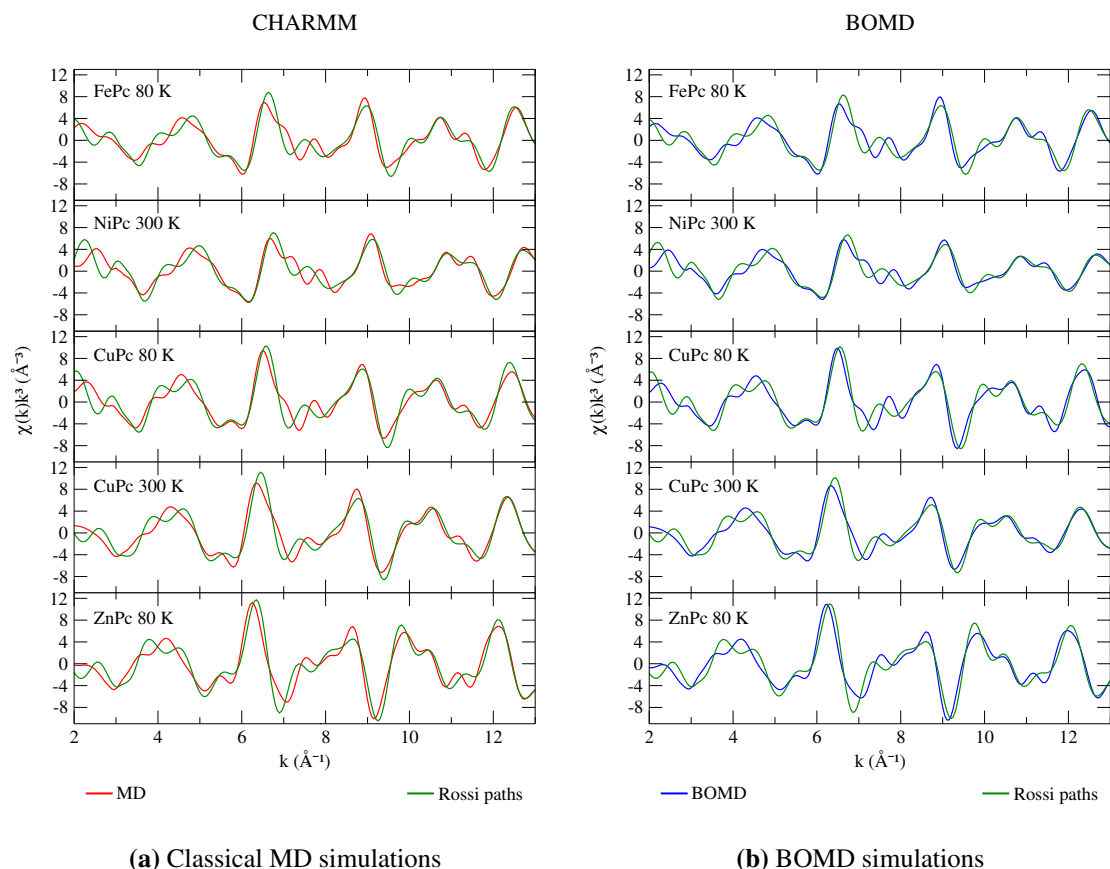


Figure 4.15: Average EXAFS spectra selecting paths vs total average EXAFS spectra. On the left, for classical MD simulations and on the right, for BOMD simulations.

case, around 60 contributions to the total spectrum because of the intrinsic degeneracy of some of the paths.

Making experimental fittings without knowing *a priori* how many paths are necessary and their relevance is an extremely difficult task. In other types of systems, as in the case of ions in solution or small molecules, 10-12 paths would be more than enough, but since any MPc is a very rigid molecule with a considerable high number of atoms, this task becomes too complicated. The use of theoretical information would greatly facilitate the work and would lead to more accurate fittings.

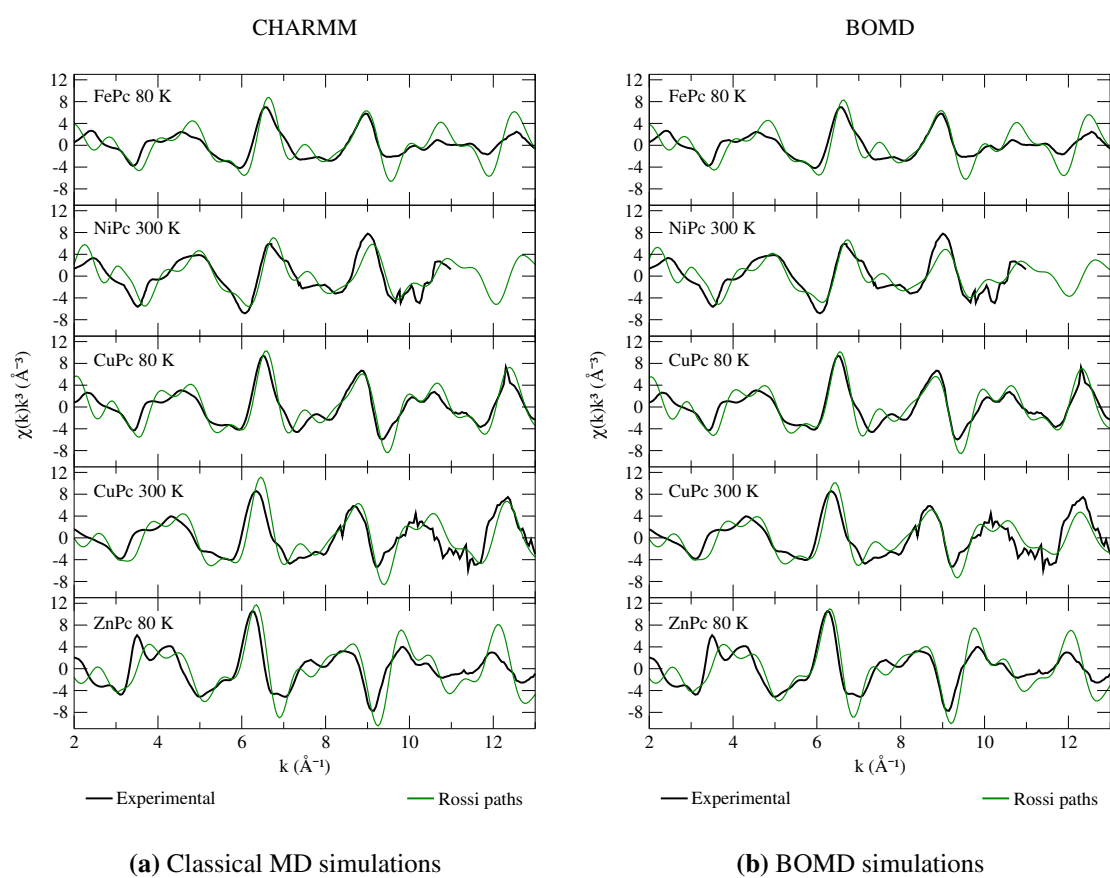


Figure 4.16: Average EXAFS spectra selecting paths vs experimental EXAFS spectra. On the left, for classical MD simulations and on the right, for BOMD simulations.

CHAPTER 5

Conclusions

The complexity and rigidity of MPCs, together with the sensitivity of EXAFS to minor structural changes, makes it a good test-bed for the development of theoretical strategies due to the numerous difficulties in the spectra fitting.

The first conclusion is that the experimental spectra are reasonably well reproduced by the original force field used. However, some features were not present in the theoretical spectra. For that reason, some changes in the original force field for ZnPc were introduced, reaching a better agreement between experiment and theory. This result reveals the sensitivity of EXAFS spectroscopy in the determination of the close environment of the absorber atom. Furthermore, it was the starting point for the extrapolation of the methodology to other MPCs, since the changes essentially occur in the region close to the metal.

As a check, the results of the BOMD simulations were compared with the results of the classical MD simulations. After verifying that a simulation time of 5 ps was enough to have temporarily converged results, it has been seen that, with two different computational levels of calculations, equivalent results have been reached.

The concept of model structure has been evaluated and, at least in this case, from a theoretical perspective, it has been possible to check the validity of a computationally less expensive strategy of generating spectra with a previous selection of backscattering paths, that is, without the need of computing average spectra. Whether this strategy is the most straightforward one depends on the ability of choosing all the relevant scattering contributions. For the MPCs systems it is shown that this is not the case.

The evolution in the interference pattern, observed when the number of shells and legs in scattering paths was increased, is complicated due to the large number of contributions with different frequencies (a function of the different effective distances) to consider.

The goodness of the approximations made by the experimentalists to reduce the number of free parameters in the fitting process (relationships between DW factors of MS and SS ones) were checked on the basis of our theoretical results, concluding that they were very reasonable although the MS paths involving the closest atoms to the absorber exhibit higher deviations (vibrations strongly correlated with ring motion).

Taking into account the amplitude of the EXAFS oscillations, it can be concluded that the theoretical DW factors are systematically smaller than the experimental ones. In addition to the limitations present in the theoretical strategy, the discrepancy between the experimental and theoretical DW factors is partly due to the lack of scattering paths included in the fitting (due to the restrictions concerning the number of parameters that can be fitted). This fact is then compensated by higher fitted DW factors in the considered contributions. In addition, there are still unresolved issues related to the intensity of the theoretical EXAFS spectra, such as the high intensity obtained in some of the MPcs, or the high intensity at high k values of others. It should be noted that, despite these discrepancies, the determination of the distances from the absorber atom to the backscattering ones is not affected, showing the robustness of the technique to the geometrical information (average distances).

One of the possible steps to follow would be the modification of the effective force constants to give accurate frequencies for the normal modes that involve the metal region. In the work of Z. Liu et al.,⁷⁰ the tendencies of the different metal-substituted MPcs in molecular, electronic and vibrational structure are studied. They demonstrated with the assignment of IR and Raman frequencies that the absorption bands which are metal dependent show a definite trend with the variation of the substituted metal, while most of the vibrational modes do not show significant shifts with metal ion.

CHAPTER 6

Bibliography

- [1] G. De La Torre, C. G. Claessens, and T. Torres, “Phthalocyanines: Old Dyes, New Materials. Putting Color in Nanotechnology,” *Chemical Communications*, 20, 2000–2015, 2007.
- [2] M. Y. Ogawa, J. Martinsen, S. M. Palmer, J. L. Stanton, J. Tanaka, R. L. Greene, B. M. Hoffman, and J. A. Ibers, “Cu(Pc)I: A Molecular Metal With A One-dimensional Array of Local Moments Embedded In A “Fermi Sea” of Charge Carriers,” *Journal of the American Chemical Society*, vol. 109, 4, 1115–1121, 1987.
- [3] V. Mastryukov, C. Ruan, M. Fink, Z. Wang, and R. Pachter, “The molecular structure of copper- and nickel-phthalocyanine as determined by gas-phase electron diffraction and ab initio/DFT computations,” *Journal of Molecular Structure*, vol. 556, 225–237, 2000.
- [4] C. J. Brown, “Crystal structure of β -copper phthalocyanine,” *Journal of the Chemical Society A: Inorganic, Physical, Theoretical*, 0, 2488–2493, 1968.
- [5] K. M. Kadish, K. M. Smith, and R. Guilard, *The Porphyrin Handbook*, vol. 11. Elsevier, 2003.
- [6] G. A. Melson, *Coordination Chemistry of Macrocyclic Compounds*. Boston, MA: Springer US, 1979.
- [7] D. K. Cabbiness and D. W. Margerum, “Macrocyclic Effect on the Stability of Copper(II) Tetramine Complexes,” *Journal of the American Chemical Society*, vol. 91, 23, 6540–6541, 1969.

- [8] G. Dufour, C. Poncey, F. Rochet, H. Roulet, S. Iacobucci, M. Sacchi, F. Yubero, N. Motta, M. Piancastelli, A. Sgarlata, and M. De Crescenzi, "Metal phthalocyanines (MPc, M=Ni, Cu) on Cu(001) and Si(001) surfaces studied by XPS, XAS and STM," *Journal of Electron Spectroscopy and Related Phenomena*, vol. 76, C, 219–224, 1995.
- [9] M. Kanai, T. Kawai, K. Motai, X. Wang, T. Hashizume, and T. Sakura, "Scanning tunneling microscopy observation of copper-phthalocyanine molecules on Si(100) and Si(111) surfaces," *Surface Science*, vol. 329, 3, L619–623, 1995.
- [10] H. R. N. Motta, A. Sgarlata, and M. D. Crescenzi, "Copper Phthalocyanine on Si (111)-7x7 and Si (001)-2x1: an XPS/AES and STM Study," *Surface Science*, vol. 319, 94, 10–20, 1994.
- [11] T. Okajima, H. Fujimoto, M. Sumitomo, T. Araki, E. Ito, H. Ishii, Y. Ouchi, and K. Seki, "Soft X-ray absorption spectra of the lithium phthalocyanine radical," *Surface Review and Letters*, vol. 09, 01, 441–446, 2002.
- [12] R. G. Jones, "X-ray Absorption: Principles, Applications, Techniques of EXAFS, SEXAFS, and XANES," *Endeavour*, vol. 12, 4, 195, 1988.
- [13] A. Muñoz-Páez and E. Sánchez Marcos, "Molecular Structure of Solvates and Coordination Complexes in Solution as Determined with EXAFS and XANES," in *Comprehensive Inorganic Chemistry II* (J. Reedijk and K. Poeppelemeier, eds.), 133–159, Amsterdam: Elsevier, 2013.
- [14] D. E. Sayers, E. A. Stern, and F. W. Lytle, "New Technique for Investigating Non-crystalline Structures: Fourier Analysis of the Extended X-Ray Absorption Fine Structure," *Physical Review Letters*, vol. 27, 18, 1204–1207, 1971.
- [15] F. Carrera, E. Sánchez Marcos, P. J. Merklings, J. Chaboy, and A. Muñoz-Páez, "Nature of metal binding sites in Cu(II) complexes with histidine and related N-coordinating ligands, as studied by EXAFS," *Inorganic Chemistry*, vol. 43, 21, 6674–6683, 2004.
- [16] G. Rossi, F. D'Acapito, L. Amidani, F. Boscherini, and M. Pedio, "Local environment of metal ions in phthalocyanines: K-edge X-ray absorption spectra," *Physical Chemistry Chemical Physics*, vol. 18, 34, 23686–23694, 2016.

- [17] J. Hong, T. J. Fauvell, W. Helweh, X. Zhang, and L. X. Chen, "Investigation of the photoinduced axial ligation process in the excited state of nickel(II) phthalocyanine," *Journal of Photochemistry and Photobiology A: Chemistry*, vol. 372, 270–278, 2019.
- [18] P. J. Merklings, A. Muñoz-Páez, and E. Sánchez Marcos, "Exploring the Capabilities of X-Ray Absorption Spectroscopy for Determining the Structure of Electrolyte Solutions: Computed Spectra for Cr^{3+} or Rh^{3+} in Water Based on Molecular Dynamics," *Journal of the American Chemical Society*, vol. 124, 36, 10911–10920, 2002.
- [19] E. C. Beret, K. Provost, D. Müller, and E. Sánchez Marcos, "Coupling CP-MD Simulations and X-ray Absorption Spectroscopy: Exploring the Structure of Oxaliplatin in Aqueous Solution," *Journal of Physical Chemistry B*, vol. 113, 36, 12343–12352, 2009.
- [20] R. Ayala, J. M. Martínez, R. R. Pappalardo, K. Refson, and E. Sánchez Marcos, "Effect of Basicity on the Hydrolysis of the Bi(III) Aqua Ion in Solution: An Ab Initio Molecular Dynamics Study," *Journal of Physical Chemistry A*, vol. 122, 7, 1905–1915, 2018.
- [21] S. Pérez-Conesa, J. M. Martínez, R. R. Pappalardo, and E. Sánchez Marcos, "Extracting the Americyl Hydration from an Americium Cationic Mixture in Solution: A Combined X-ray Absorption Spectroscopy and Molecular Dynamics Study," *Inorganic Chemistry*, vol. 57, 14, 8089–8097, 2018.
- [22] C. Shao, Y. Jin, K. Pipe, M. Shtein, and J. Kieffer, "Simulation of Crystalline and Amorphous Copper Phthalocyanine: Force Field Development and Analysis of Thermal Transport Mechanisms," *Journal of Physical Chemistry C*, vol. 118, 19, 9861–9870, 2014.
- [23] P. J. Dwyer, R. J. Vander Valk, V. Caltaldo, D. Demianicz, and S. P. Kelty, "All-atom charmm force field and bulk properties of perfluorozinc phthalocyanines," *The Journal of Physical Chemistry A*, vol. 118, 49, 11583–11590, 2014.
- [24] A. R. Leach, *Molecular Modelling: Principles and Applications*. Harlow: Pearson education Limited, second ed., 2001.

- [25] B. R. Brooks, R. E. Bruccoleri, B. D. Olafson, D. J. States, S. a. Swaminathan, and M. Karplus, "Charmm: a program for macromolecular energy, minimization, and dynamics calculations," *Journal of computational chemistry*, vol. 4, 2, 187–217, 1983.
- [26] S. Nosé, "A unified formulation of the constant temperature molecular dynamics methods," *The Journal of Chemical Physics*, vol. 81, 1, 511–519, 1984.
- [27] W. G. Hoover, "Canonical dynamics: Equilibrium phase-space distributions," *Physical Review A*, vol. 31, 3, 1695–1697, 1985.
- [28] J. E. Penner-Hahn, "X-ray absorption spectroscopy in coordination chemistry," *Coordination Chemistry Reviews*, vol. 190-192, 1101–1123, 1999.
- [29] K. Bolton, W. L. Hase, and G. H. Peslherbe, "Direct dynamics simulations of reactive systems," in *Modern Methods for Multidimensional Dynamics Computations in Chemistry*, 143–189, World Scientific, 1998.
- [30] A. Warshel and M. Karplus, "Calculation of ground and excited state potential surfaces of conjugated molecules. I. formulation and parametrization," *Journal of the American Chemical Society*, vol. 94, 16, 5612–5625, 1972.
- [31] R. Car and M. Parrinello, "Unified approach for molecular dynamics and density-functional theory," *Physical review letters*, vol. 55, 22, 2471, 1985.
- [32] H. Hellman, "Einführung in die quantenchemie," *Franz Deuticke, Leipzig*, vol. 285, 1937.
- [33] R. P. Feynman, "Forces in molecules," *Phys. Rev.*, vol. 56, 340–343, 1939.
- [34] R. Car, F. Angelis, P. Giannozzi, and N. Marzari, *First-Principles Molecular Dynamics*, 59–76. 2005.
- [35] P. Kramer and M. Saraceno, "Geometry of the time-dependent variational principle in quantum mechanics," in *Group theoretical methods in physics*, 112–121, Springer, 1980.
- [36] R. d. L. Kronig, "Zur Theorie der Feinstruktur in den Röntgenabsorptionsspektren. III," *Zeitschrift für Physik*, vol. 75, 7, 468–475, 1932.

- [37] J. A. van Bokhoven and C. Lamberti, *X-Ray Absorption and X-Ray Emission Spectroscopy*, vol. 1-2. Chichester, UK: John Wiley & Sons, 2016.
- [38] G. S. Henderson, D. R. Neuville, and R. T. Downs, *Spectroscopic Methods in Mineralogy and Materials Sciences*, vol. 78. 2015.
- [39] J. E. Müller and J. W. Wilkins, “Band-structure Approach to the X-ray Spectra of Metals,” *Physical Review B*, vol. 29, 8, 4331–4348, 1984.
- [40] B. K. Teo, *EXAFS: Basic Principles and Data Analysis*, vol. 9 of *Inorganic Chemistry Concepts*. Berlin, Heidelberg: Springer Berlin Heidelberg, 1986.
- [41] C. A. Ashley and S. Doniach, “Theory of Extended X-ray Absorption Edge Fine Structure (EXAFS) in Crystalline Solids,” *Physical Review B*, vol. 11, 4, 1279–1288, 1975.
- [42] P. A. Lee and J. B. Pendry, “Theory of the Extended X-ray Absorption Fine Structure,” *Physical Review B*, vol. 11, 8, 2795–2811, 1975.
- [43] F. Jalilehvand, *Structure of Hydrated Ions and Cyanide Complexes by X-Ray Absorption Spectroscopy*. PhD thesis, University of Calgary, 2000.
- [44] F. M. Carrera López, *Estudio de la estructura en disolución de complejos de elementos de transición relacionados con sistemas de interés biológico mediante Espectroscopía de Absorción de Rayos X*. PhD thesis, Universidad de Sevilla, 2005.
- [45] J. J. Rehr, E. A. Stern, R. L. Martin, and E. R. Davidson, “Extended X-ray Absorption Fine Structure Amplitudes Wave-function Relaxation and Chemical Effects,” *Physical Review B*, vol. 17, 2, 560–565, 1978.
- [46] J. J. Rehr and R. C. Albers, “Theoretical Approaches to X-ray Absorption Fine Structure,” *Reviews of Modern Physics*, vol. 72, 3, 621–654, 2000
- [47] Y. Joly, D. Cabaret, H. Renevier, and C. R. Natoli, “Electron Population Analysis by Full-Potential X-Ray Absorption Simulations,” *Physical Review Letters*, vol. 82, 11, 2398–2401, 1999.
- [48] A. J. H. Wachters, “Gaussian basis set for molecular wavefunctions containing third-row atoms,” *The Journal of Chemical Physics*, vol. 52, 3, 1033–1036, 1970.

- [49] P. J. Hay, "Gaussian basis sets for molecular calculations. the representation of 3d orbitals in transition-metal atoms," *The Journal of Chemical Physics*, vol. 66, 10, 4377–4384, 1977.
- [50] K. Raghavachari and G. W. Trucks, "Highly correlated systems. excitation energies of first row transition metals Sc–Cu," *The Journal of Chemical Physics*, vol. 91, 2, 1062–1065, 1989.
- [51] U. C. Singh and P. A. Kollman, "An approach to computing electrostatic charges for molecules," *Journal of Computational Chemistry*, vol. 5, 2, 129–145, 1984.
- [52] B. H. Besler, K. M. Merz Jr., and P. A. Kollman, "Atomic charges derived from semiempirical methods," *Journal of Computational Chemistry*, vol. 11, 4, 431–439, 1990.
- [53] J. Tao, J. P. Perdew, V. N. Staroverov, and G. E. Scuseria, "Climbing the density functional ladder: Nonempirical meta-generalized gradient approximation designed for molecules and solids," *Phys. Rev. Lett.*, vol. 91, 146401, 2003.
- [54] Q. Du, X. Wu, P. Wang, D. Wu, L. Sai, R. B. King, S. J. Park, and J. Zhao, "Structure evolution of transition metal-doped gold clusters $M@Au^{12}$ ($M = 3d-5d$): Across the periodic table," *The Journal of Physical Chemistry C*, vol. 124, 13, 7449–7457, 2020.
- [55] F. Neese, F. Wennmohs, U. Becker, and C. Riplinger, "The orca quantum chemistry program package," *The Journal of Chemical Physics*, vol. 152, 22, 224108, 2020.
- [56] W. Smith and T. R. Forester, "DL POLY 2.0: A general-purpose parallel molecular dynamics simulation package," *Journal of Molecular Graphics*, vol. 14, 3, 136–141, 1996.
- [57] H. J. Berendsen, J. v. Postma, W. F. Van Gunsteren, A. DiNola, and J. R. Haak, "Molecular dynamics with coupling to an external bath," *The Journal of chemical physics*, vol. 81, 8, 3684–3690, 1984.
- [58] G. J. Martyna, M. L. Klein, and M. Tuckerman, "Nosé–hoover chains: The canonical ensemble via continuous dynamics," *The Journal of chemical physics*, vol. 97, 4, 2635–2643, 1992.

- [59] G. J. Martyna, M. E. Tuckerman, D. J. Tobias, and M. L. Klein, “Explicit reversible integrators for extended systems dynamics,” *Molecular Physics*, vol. 87, 5, 1117–1157, 1996.
- [60] J. J. Rehr, J. J. Kas, F. D. Vila, M. P. Prange, and K. Jorissen, “Parameter-free calculations of X-ray spectra with FEFF9,” *Physical Chemistry Chemical Physics*, vol. 12, 21, 5503–5513, 2010.
- [61] R. Ayala, E. S. Marcos, S. Díaz-Moreno, V. A. Solé, and A. Muñoz-Páez, “Geometry and hydration structure of Pt(II) square planar complexes $[\text{Pt}(\text{H}_2\text{O})_4]^{2+}$ and $[\text{PtCl}_4]^{2-}$ as studied by X-ray absorption spectroscopies and quantum-mechanical computations,” *The Journal of Physical Chemistry B*, vol. 105, 31, 7588–7593, 2001.
- [62] F. Carrera, E. S. Marcos, P. J. Merkling, J. Chaboy, and A. Muñoz-Páez, “Nature of metal binding sites in Cu(II) complexes with histidine and related n-coordinating ligands, as studied by EXAFS,” *Inorganic Chemistry*, vol. 43, 21, 6674–6683, 2004.
- [63] K. Provost, E. C. Beret, D. B. Muller, A. Michalowicz, and E. S. Marcos, “EXAFS Debye-Waller factors issued from Car-Parrinello molecular dynamics: Application to the fit of oxaliplatin and derivatives,” *The Journal of Chemical Physics*, vol. 138, 8, 084303, 2013.
- [64] D. Z. Caralampio, J. M. Martínez, R. R. Pappalardo, and E. S. Marcos, “Development of a polarizable and flexible model of the hydrated ion potential to study the intriguing case of Sc(III) hydration,” *Theoretical Chemistry Accounts*, vol. 136, 4, 1–8, 2017.
- [65] T. Yokoyama, K. Kobayashi, T. Ohta, and A. Ugawa, “Anharmonic interatomic potentials of diatomic and linear triatomic molecules studied by extended X-ray absorption fine structure,” *Physical Review B*, vol. 53, 10, 6111–6122, 1996.
- [66] D. Haskel, *Local Structural Studies of Oriented High Temperature Superconducting Cuprates by Polarized XAFS Spectroscopy*. PhD thesis, University of Washington, Seattle, 1998.

- [67] S. H. Kim, O. Toshiaki, and G. H. Gang, "In situ structural investigation of iron phthalocyanine monolayer adsorbed on electrode surface by X-ray absorption fine structure," *Bulletin of the Korean Chemical Society*, vol. 21, 6, 588–594, 2000.
- [68] H. J. Choi, G. Kwag, and S. Kim, "Electrochemical and XAFS investigation of nitrite reduction by heat-treated μ -oxo derivative of iron phthalocyanine supported on high area carbon," *Journal of Electroanalytical Chemistry*, vol. 508, 1-2, 105–114, 2001.
- [69] G. Raposo-Hernández, J. M. Martínez, R. R. Pappalardo, C. Den Auwer, and E. Sánchez Marcos, "A coupled EXAFS-molecular dynamics study on PuO_2^+ and NpO_2^+ hydration: The importance of electron correlation in force-field building," *Inorganic Chemistry*, vol. 61, 23, 8703–8714, 2022.
- [70] Z. Liu, X. Zhang, Y. Zhang, and J. Jiang, "Theoretical investigation of the molecular, electronic structures and vibrational spectra of a series of first transition metal phthalocyanines," *Spectrochimica Acta Part A: Molecular and Biomolecular Spectroscopy*, vol. 67, 5, 1232–1246, 2007.